Ion Temperature Measurements on the HL-2A Tokamak using a Retarding Field Analyser

A Thesis Submitted to the

College of Graduate Studies and Research

in Partial Fulfillment of the Requirements

for the degree of Master of Science

in the Department of Physics and Engineering Physics

University of Saskatchewan

Saskatoon

By

L. Kurt Kreuger

PERMISSION TO USE

In presenting this thesis in partial fulfilment of the requirements for a Postgraduate degree from the University of Saskatchewan, I agree that the Libraries of this University may make it freely available for inspection. I further agree that permission for copying of this thesis in any manner, in whole or in part, for scholarly purposes may be granted by the professor or professors who supervised my thesis work or, in their absence, by the Head of the Department or the Dean of the College in which my thesis work was done. It is understood that any copying or publication or use of this thesis or parts thereof for financial gain shall not be allowed without my written permission. It is also understood that due recognition shall be given to me and to the University of Saskatchewan in any scholarly use which may be made of any material in my thesis.

Requests for permission to copy or to make other use of material in this thesis in whole or part should be addressed to:

Head of the Department of Physics and Engineering Physics
University of Saskatchewan
Saskatoon, Saskatchewan S7N 5E2

ABSTRACT

World energy demands are increasing while the ability to generate that energy currently requires relying on non-renewable, and increasingly unsustainable, sources. If this trend is going to be curbed, either the energy demands will have to be limited, or new methods of sustainable energy need to be found. The former option is beyond the scope of this research so focus here is on new energy sources.

Nuclear fusion is a possible option due to the output energy possible and the ease of access to fuel. Radioactive byproducts are also very limited. The tokamak uses magnetic fields to achieve fusion conditions and is one of the leading contenders for a working fusion reactor.

The topic of this research is the construction of a probe used on the tokamak to measure ion temperature in the edge region of the plasma. A model was also constructed to aid in the interpretation of experimental data. The probe itself was constructed, along with the electrical circuits required for its operation, in Hefei, China, and was mounted on a reciprocating drive on the HL-2A tokamak in Chengdu, China. Reciprocation allowed for the construction of an ion temperature profile.

A profile was constructed showing the evolution of temperature throughout a single shot. However, due to some noise constraints on the data, another profile was constructed averaging several shots together. This increased the quality of the temperature data at the expense of seeing how temperature changes over single shots.

To address some issues related to this probe, an improved probe was designed and constructed. It is currently being used on the superconducting EAST tokamak in Hefei, China.

ACKNOWLEDGEMENTS

It takes many names for a project like this to be finished. Mine just happens to be the one on the cover. Firstly, I'd like to thank my supervisor, Dr. Chijin XIAO, who has provided continual support. His patience and guidance while I worked through the many theoretical and practical questions I had throughout this whole process was a key reason this project came to fruition. It was also because of him that I was able to live in China for several months doing this research. That time is very special to me.

In Hefei, China, there were many people who provided all sorts of help. Ms. Min JIANG, a fellow Master's student at the time, was always there to not only help me with communicating with local specialists in the design and construction of this project, but helped me along as I lived in a vastly different cultural environment. Huiqian WANG, among many other things, shared his valuable experience in the various lab equipment necessary for an experiment of this type. Dr. Wei ZHANG also provided guidance and support for my many questions. Dr. Guosheng XU was there serving me as a kind of supervisor-at-a-distance. And Mr. YUAN was as capable in the machine shop as he was patient with the need for interpreters. It is quite difficult for me to narrow down what each of these people did individually because, really, they did so much. Their support as a group was invaluable. A Master's degree is one of the first relatively intense research experiences for a student, so there is already lots of learning taking place. Combine that with a research environment in a cultural setting drastically different from one's own, and the importance of a strong support network is seen. These wonderful people provided that network, and for that, I am exceedingly grateful.

In Chengdu, where the project was actually implemented and data taken, Defeng KONG and Zhihui HUANG were of special importance. As fellow graduate students, they had their own research to handle but were both always exceedingly willing to help a bumbling Canadian student with little knowledge and experience researching on this level.

The other students from the research group in Saskatoon also were instrumental in this project. Sayf Elgriw, a friend and a colleague, offered the experience of having been a Master's student in this lab before. Kyam M Thu, whose project had many similarities, helped me visualize the steps I would need to take. Mykola Dreval (Nick) provided his years of experience in the field with some key support. David McColl, an Engineer in the lab, seemed to never tire of my questions.

Dr. Akira Hirose and Dr. Rob Pywell, for serving on my committee, deserve a great thanks. They have graciously offered their time away from their other responsibilities as professors and researchers to ensure this project maintains a high degree of scientific integrity and value.

An acknowledgements section can't be complete without thanking one's parents. Mine have always been there to remind me of what's important when I stumble a bit. They have provided encouragement, praise, answers, questions, all when I needed it most. Words cannot express the degree of appreciation I feel.

Of course there are many many others that helped me through this process, but I am not able to name them all. In my ignorance, I'm sure there are also many who helped without my seeing it. For the silent helpers, the brief encounters with the right person at the right time, the small but significant pieces of thought and idea in hallway conversations, for just being my friend, thank you to everyone. I hope and pray that I am able to be there for others in the same spirit as others were there for me.

And even though it doesn't always garner a thanks of the same length, "funding" is a magic word to graduate students, without which I would not have been able to complete this project. I am very appreciative of the University of Saskatchewan as well as NSERC for providing this perhaps mundane but very important support. Thank you.

CONTENTS

LIST OF FIGURES

LIST OF ABBREVIATIONS AND SYMBOLS

RFA	Retarding Field Analyser
SOL	Scrape off layer
TEM grids	Transmission Electron Microscopy grids - used as grids in the RFA
ES A	Entrance slit for probe A
ES B	Entrance slit for probe B
G1 A	Grid 1 for probe A
G1 B	Grid 1 for probe B
G2 A	Grid 2 for probe A
G2 B	Grid 2 for probe B
Col A	Collector plate for probe B
Col B	Collector plate for probe B
MHD	Magnetohydrodynamics - in this case it refers to the diagnostic signal
DAQ	Data Acquisition
JET	Joint European Torus - large tokamak in the UK
HL-2A	Tokamak in Chengdu, China - location of this research project
EAST	Experimental Advanced Superconducting Tokamak - located in Hefei, China
JFT-2M	Tokamak in Japan
STOR-M	Saskatchewan Tokamak Modified - tokamak at the U of S
Tore Supra	Tokamak in France
L-mode	Low confinement mode - Standard mode of tokamak operation
H-mode	High confinement mode - Mode indicative of substantially improved confinement times
v	Particle velocity - subscripts $\perp$ and $\parallel$ indicate directions perpendicular and parallel to the magnetic field, respectively. Subscript *th* indicates thermal velocity
n	Particle density
τ_e	Energy confinement time
T_i	Ion temperature
T_e	Electron temperature
λ_D	Debye length
r_L	Larmor radius
a	Radius of probe
l	Length of probe

CHAPTER 1

INTRODUCTION

1.1 Nuclear Fusion Energy

The world is currently experiencing a dramatic increase in energy demands, most of which are being satisfied by burning fossil fuels. Figure 1.1 shows that the three largest energy sources by far come from petroleum, coal, and natural gas [1].

There are many concerns in using fossil fuels at the current rate. One of the most obvious issues is related to carbon dioxide production. Carbon dioxide concentrations are regulated by natural processes, such as plant photosynthesis [2]. However, due to the burning of fossil fuels, more carbon dioxide is being introduced into the natural cycle than is being absorbed. Given that carbon dioxide is a greenhouse gas, it is likely a significant factor in the warming of the Earth's climate over the last century [2].

Fossil fuels are also dangerous for organic life. For example, petroleum, one of the main fossil fuels, is highly toxic. Oil in water at concentrations of as little as 4000ppm is "acutely lethal" to fish [3].

Aside from adverse health affects, fossil fuels are non-renewable. With rising demand and a diminishing supply, costs will inevitably go up.

From Fig. 1.1, only 14% of the world's energy supply currently comes from non-fossil fuels, which includes fission based nuclear electric power and renewable sources such as hydroelectric, solar, and wind. Nuclear power generated through a fusion process has the potential to provide a safe, inexpensive, and abundant energy supply for the world.

Fusion is the general process by which two smaller nuclei come together to form a heavier nucleus. There are many different atomic species that can theoretically undergo a fusion reaction which releases energy. A common example is that of deuterium (D) and tritium (T), two

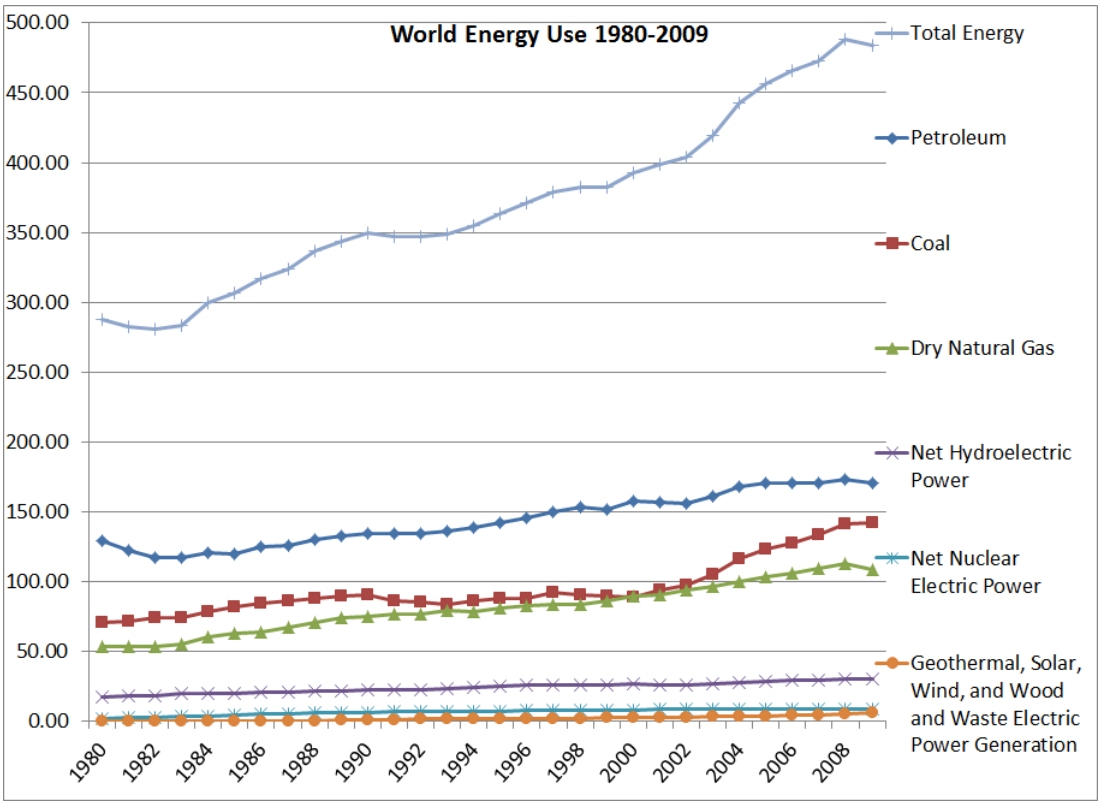

Figure 1.1: World energy use broken up into various main sources.

isotopes of hydrogen. Their nuclear reaction is described by:

$$D + T \rightarrow {}^{4}_{2}He(3.5\text{MeV}) + n(14.1\text{MeV}) \tag{1.1}$$

Here is where the reason for fusion being considered as an energy source is seen - 17.6MeV energy release per D-T pair [4]. Also, unlike nuclear fission, no radioactive products are generated in this process. The only radioactivity that is generated here comes from the neutron interacting with fusion machine components. However, the radioactive products are short-term, and the technology has little in common with nuclear weapons technology.

What stops fusion from occurring in many natural situations is called the *Coulomb* barrier. Both nuclei are positively charged, so they repel each other. The closer these nuclei are brought together, the stronger the repulsive force. Another force, stronger than the electric repulsion, is needed for fusion to occur. This force is the strong nuclear force - that force responsible for holding the nucleus together. It is substantially stronger than the electromagnetic repulsion, but only over a very small distance. Once the particles approach each other at this distance, fusion can occur. This can happen if two particles have a head-on collision with each other at a high

enough speed, or high enough temperature. At the temperatures required for fusion reactions, the gas that would be used as fuel becomes ionized, and a plasma is created. Plasma is the fourth state of matter in addition to solid, liquid, and gas, and details of its behaviour will be discussed in the next section.

Fusion is an exothermic reaction, meaning that more energy is released by the reaction than is required to sustain it. Some of the output energy can be recycled back into maintaining necessary fusion conditions, temperature being one of those conditions. Density and energy confinement time form the remaining components of the *fusion triple product*. A self-sustaining fusion reaction is achieved when this product is above a minimum value [5]:

$$n\tau_e T > 3.4 \times 10^{21} \mathrm{m}^{-3}\mathrm{s\ keV} \tag{1.2}$$

where n is the density, τ_e is the energy confinement time - defined as the ratio between the thermal energy density of the plasma volume and the power loss density, and T is the temperature. The higher the density and confinement time at a sufficiently high temperature, the higher the chances of a collision resulting in a fusion reaction. One approach to confining plasma at sufficiently high temperatures - in the hundreds of millions of degrees centigrade - is to use strong magnetic fields. Fusion in this fashion is termed *magnetic fusion* and the tokamak is one of the most promising configurations.

1.2 Plasma Basics

Since a plasma results from the temperatures needed for fusion, it would be useful at this juncture to discuss some of the plasma properties directly related to this M.Sc. research project. A plasma, as an ionized gas, contains many charged particles. Charged particles respond in complex ways to external magnetic fields, therefore, the first idea to discuss is how a single ion behaves in an external magnetic field. Since solid conducting surfaces regularly come into contact with plasmas, either as the containing device, or probes inserted into the plasma, the second idea presented is about how plasmas react to these solid objects.

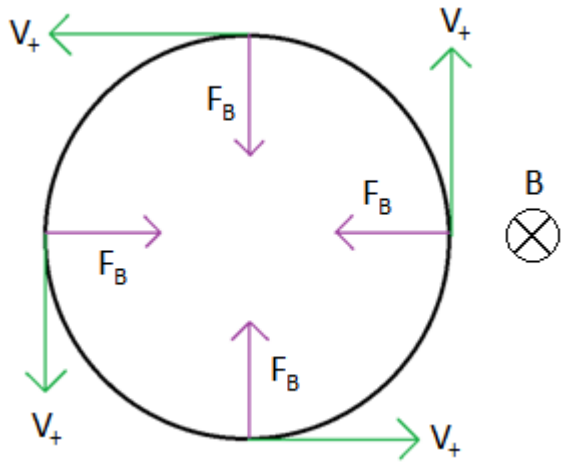

Figure 1.2: The magnetic field is into the page and uniform. The arrows labeled V_+ are possible velocities in this plane for a particle of charge $+q$, and the arrows labeled F_B are the resulting Lorentz forces. The result is a circular trajectory with radius equal to the Larmor radius.

1.2.1 Larmor Motion

As a charged particle of mass m moves in a magnetic field $\vec{B}$ with velocity $\vec{v}$, it experiences a Lorentz force, which is perpendicular to both the velocity and the magnetic field. This force is given by $\vec{F} = q\vec{v} \times \vec{B}$ where q is the particle charge. Any motion in the direction of the magnetic field is unaffected by this force. Figure 1.2 shows how this force leads to a circular path, in a uniform magnetic field, when considering only velocities in the plane perpendicular to the magnetic field $v_\perp$. To find the radius r of this orbit, it is recognized that the magnetic force holding this circular motion pattern is equal to the centrifugal force of $mv_\perp^2/r$, leading to $qv_\perp B = mv_\perp^2/r$. Solving for r leads to the orbiting radius, or the Larmor radius, $r_L = mv_\perp/qB$. If the ion and electron temperatures are approximately equal, it can be shown that the ratio of ion Larmor radius r_{Li} to electron Larmor radius r_{Le} is $r_{Li}/r_{Le} = \sqrt{m_i/m_e}$, where m_i and m_e are ion and electron mass, respectively. For hydrogen plasma, this is ≈ 43. By substituting $v = \omega r$, the frequency of this orbit, called the cyclotron frequency, can be described as $\omega_c = qB/m$. It should be clear that if a charged particle is placed inside a uniform magnetic field, the motion in the direction perpendicular to $\vec{B}$ will be restricted so that it will move in a helical spiral around the magnetic field lines.

1.2.2 Debye Shielding

Since the probe will be in direct contact with a plasma, it is important to understand how the plasma will react. When an external potential is applied to a probe surface within a plasma, the plasma reorganizes itself such that the perturbing effect of this external potential is limited to within a small distance - the plasma bulk is shielded from the potential. An illustrative, though somewhat simplified, explanation for this behaviour assumes cold ions. Under this assumption, ions are essentially immobile, since they are cold and heavy compared with electrons. It is also assumed that the conducting surface is floating. Far away from the surface, the plasma is quasineutral, and the electron and ion charge densities are equal. Due to the thermal motion of the electrons in plasma, they will impinge upon the surface and be absorbed. This will occur until the surface retains a charge strong enough to repel all other electrons. The net result is a layer (called a sheath in plasma physics) around the surface where the electron density is perturbed compared with the unperturbed electron density far away from the surface. The ion density remains unchanged.

Since a net surplus of positive charges exists in the sheath, Poisson's equation is employed to determine the spatial dependence of potential.

$$\nabla^2 V = -\frac{\rho}{\varepsilon_0} = -\frac{e}{\varepsilon_0}(n_i - n_e) \tag{1.3}$$

where n_i, e, n_e, and ρ is the ion density, magnitude of the electron charge, electron density, and total charge density, respectively. Singly charged ions are assumed. The function often used to describe the electron density, n_e, in terms of electric potential in this region involves the Boltzmann distribution:

$$n_e = n_\infty \exp\left(\frac{eV}{T_e}\right). \tag{1.4}$$

Far from the probe, the plasma is quasi-neutral. The density for both electrons and ions in this region is n_∞. T_e is the electron temperature in energy units. V is the perturbed potential around the surface. The Taylor series approximation that $\exp(eV/T_e) \approx 1 + eV/T_e$ obtains the following differential equation:

$$\nabla^2 V = \frac{1}{\lambda_D^2} V, \lambda_D^2 = \frac{\varepsilon_0 T_e}{e^2 n_\infty} \tag{1.5}$$

where λ_D is called the Debye length. The solution describes an exponentially decaying potential is space. The voltage from a perturbing potential is only seen by the plasma at a distance of the order of the Debye length. Any influence beyond this distance is effectively shielded by the plasma sheath.

1.3 Tokamak

A tokamak tries to exploit the confining nature of the Larmor motion of ions to maintain a high density, high temperature plasma for a long enough time. A plasma is created inside a chamber and an external magnetic field is applied. As discussed above, motion in the direction perpendicular to the magnetic field is confined by the Lorentz force. In the parallel direction, however, the plasma moves freely. To prevent loss of particles due to this parallel motion, the particles are confined to the closed magnetic field lines of the torus shaped chamber of a tokamak.

Because the tokamak is a torus, it is useful to define a few terms relating to the geometry. If a torus is a cylinder that has been bent into a circle, then the major radius is the radius of this circle and the *toroidal* direction points along the cylinder's main axis. The minor radius would be the radius of the cylinder itself and the *poloidal* direction curves along the edge of the circular cross section. These directions are indicated in Fig. 1.3 by the toroidal and poloidal fields.

The toroidal field is created by the toroidal field coils (see Fig. 1.3). To understand how currents cause magnetic fields, take, for example, a circular coil in the plane of this page. When a current is passed through it in a clockwise direction, a magnetic field is created which goes into the page within the circle and comes out of the page outside the circle. Putting an identical coil on top of the first, carrying the same current, produces a magnetic field of twice the strength. A solenoid is a long cylinder with dense windings which induces a uniform magnetic field along the axis of the cylinder. Bending the solenoid with an axial field into a circle results in a torus with a toroidal field. Thus, having many coils positioned as in Fig. 1.3, a toroidal field can be created.

A problem arises, however, because the magnetic field produced by the toroidal coils is not

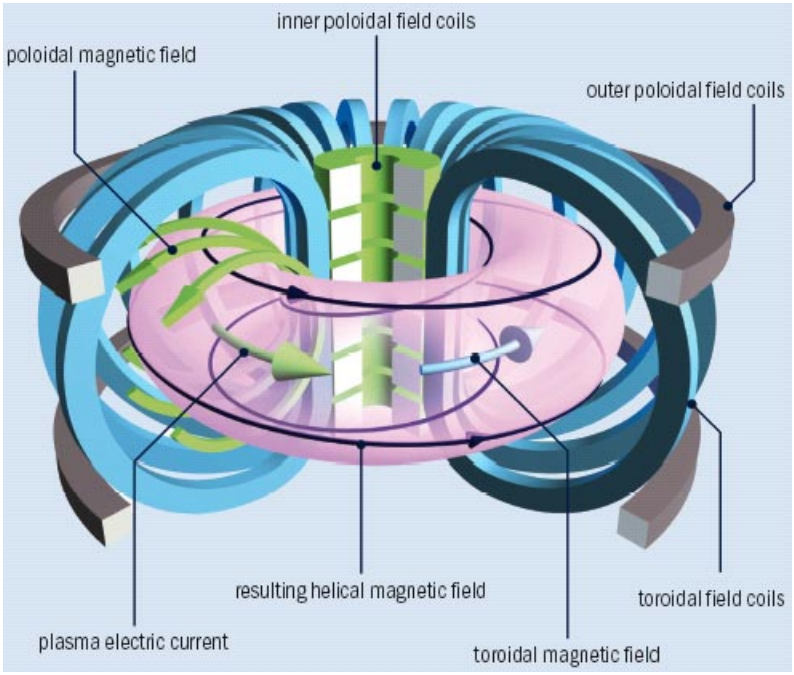

Figure 1.3: The main components of a tokamak, along with a diagram of the fields and plasma volume.

uniform. When Ampère's law is applied at various toroidal radii, r, it can be shown that B is proportional to $1/r$. What develops, then, is stronger magnetic field near the inner poloidal field coils and a weaker field near the outer coils. Whenever a gradient exists in a magnetic field, the Larmor motion is no longer circular because the radius of orbit is related to the magnetic field strength. For example, consider an ion in Larmor motion in a non-uniform field. While it is in the stronger field, it will have a certain Larmor radius. As it continues to orbit, it will enter a weaker field and the Larmor radius increases. The net result is a *grad B* drift, proportional to $\nabla\vec{B}\times\vec{B}$. The curved magnetic field lines also result in a curvature drift. Both drifts are charge dependant and perpendicular to both the gradient (outward in Fig. 1.3) and the toroidal motion. Positive charges drift upward in the configuration shown in Fig. 1.3, and negative charges drift downward.

The separation of charges continues until the newly created electric field is strong enough to oppose the drift. However, because of this electric field, another similar drift occurs due to the speed dependence of the Larmor radius. When accelerated by the electric field, the particle's Larmor radius will increase. It will decrease at the other side of the orbit, where the electric field decelerates the particle. This drift is called the $E\times B$ drift. The drift direction,

independent of the sign of the charge polarity, is outward, in the same direction as the $\vec{E} \times \vec{B}$ vector. Through these mechanisms, confinement time is dramatically reduced as particles drift into the chamber walls.

A helical field, as shown in Fig. 1.3, serves to eliminate the $E \times B$ drift. This field is created by a superposition of the toroidal and poloidal fields (each labeled in Fig. 1.3). The magnetic field gradient is unchanged because the poloidal field is small compared to the toroidal field, so the grad B drift remains. However, while following the helical field lines, the charges at the top are brought down and vice versa. The charge separation that resulted from the grad B drift is effectively neutralised, thus eliminating the $E \times B$ drift.

The poloidal field is created by a large current passed through the plasma which, as a separate but important role, heats the plasma through ohmic heating. The inner poloidal coils are used to induce this current in the plasma by acting as the primary winding of a transformer, the plasma itself acting as the secondary winding. Due to the same principles by which the toroidal field is created, this toroidal current creates a poloidal magnetic field. The outer poloidal field coils generate a vertical magnetic field which interacts with the plasma current by way of the Lorentz force to create a force inward to counteract the outward hooping force.

While the magnetic field lines at the center of the poloidal cross section are closed, at some point the field lines will intersect with a machine component. Because the field lines are now open, excessive energy will be deposited at these intersections. In part to separate the plasma from the tokamak vessel, one of two main methods is employed. In some tokamaks, a *limiter* is simply inserted into the plasma, forcing some field lines to become open. In others, magnetic field lines are manipulated so they intersect with a *divertor*. In either case, the point at which field lines go from closed to open is called the *separatrix*, beyond which is the *scrape-off layer*, or SOL. The plasma edge, less rigidly defined, is the outer few cm before the SOL.

For the interested reader, a great text with a deeper and more complete analysis of plasma physics is ref. [6]. Chapters 15 and 16 of ref. [7] analyze the tokamak itself.

1.4 Problem Formulation

Now we are at the stage where the purpose of this research project can be at least outlined. As will be shown in the next chapter, ion temperature in the edge region is a very important quantity that influences phenomena responsible for global confinement times of the plasma. Unlike with electron temperature, however, it is not so easy to measure. The RFA is the most common and widely accepted method of edge temperature measurement([8]). The first purpose of this project is to design and build an RFA and take edge region ion temperature measurements. This was done on a tokamak with no such diagnostics already in place.

One weakness to RFA measurements is the lack of independent verification using other measurement methods. As such, models play a more important role in determining the validity of RFA measurements. As far as the author knows, none of these models have taken into account the internal geometry of the probe. Chapter three discusses why measurements might be influenced by RFA geometry. The second main purpose of this project is to build such a mathematical model. The results will show that there is value in pursuing more work along these lines.

1.5 Thesis Outline

This first chapter has outlined the motivations for fusion research, some information on basic plasma physics pertaining to this research, and an brief description of the tokamak.

Chapter two will provide a background of why ion temperature measurements in the edge region are important and a brief review of several methods available. It will conclude with a more detailed description of the probe used in this research.

The third chapter details the experimental setup, including some specifics of the HL-2A tokamak.

Chapter four describes a mathematical model developed to assist in the interpretation of probe data.

Chapters five and six are devoted, respectively, to the results of this research and the conclusions reached.

CHAPTER 2

ION TEMPERATURE MEASUREMENTS IN TOKAMAKS

2.1 Importance of Ion Temperature Measurements

Implicit in the previous chapter's description of a plasma is the recognition that a plasma has both particle (or kinematic) and fluid properties, Larmor motion being an example of the former and the Debye sheath, the latter. Under certain circumstances, fluids can exhibit turbulence, which is a very poorly understood phenomenon and the primary reason for anomalous confinement significantly worse than predicted by classical and neo-classical theory.

Recent experiments in transport studies are making clearer the importance of the edge region [9]. It has been found that tokamaks can operate in what is known as high confinement mode, or *H-mode*, as opposed to low confinement, or *L-mode*. This mode is characterized by a dramatic increase in confinement times. There is the possibility of a connection between H-mode and what are known as "zonal flows" [10], which can be separated into two types: stationary zonal flows, and the Geodesic Acoustic Mode, or GAM. The frequency of the latter mode depends on ion temperature [11].

$$f_{GAM} = \sqrt{\frac{T_i + T_e}{m_i}} \frac{1}{2\pi R} \tag{2.1}$$

where R is the major radius of the tokamak (see Fig. 1.3), m_i is the ion mass, and T_i and T_e are the ion and electron temperatures, respectively.

During L- to H-mode transitions, there is a dramatic increase in the radial electric field in the edge region [12]. This increased radial electric field is connected with a shearing poloidal velocity due to $E \times B$ drift, the E_r being the electric field pointing in the radial direction, and B_T being the toroidal magnetic field. Its effect is seen in the poloidal plasma flow, which is thought

to be a reason for the decrease in edge turbulence [10]. As McKee describes, this shearing velocity breaks the turbulent eddy structures, reducing outward particle transport. The edge electron and ion temperatures affect this radial electric field through the radial force balance equation. It is given in terms of the edge plasma pressure gradient, ∇P_i, and the toroidal and poloidal velocities, $v_{\phi i}$ and $v_{\theta i}$, respectively [12].

$$E_r = \frac{\nabla P_i}{Z_i e n_i} + v_{\phi i} B_\theta - v_{\theta i} B_\phi \tag{2.2}$$

B_θ is the poloidal magnetic field and B_ϕ is the toroidal field shown in Fig. 1.3. Z_i is the degree of ionization, e is the electron charge, and n_i is the ion density. Temperature enters this equation through the pressure term $P_i = nkT_i$, where k is the Boltzmann constant.

Finally, in the edge region, ion temperature is also important for determining the amount of energy deposited onto the chamber wall, and thus, the amount of impurities released into the plasma. The impurities influence plasma stability and tokamak material choice [9].

Techniques used to measure many of the parameters that describe the above phenomena are readily available. However, the ion temperature is one that is more difficult to measure. There are many methods to measure this value, but, in the edge region of a tokamak, the Retarding Field Analyzer (RFA) is the most successful candidate. Large tokamaks present certain difficulties in employing RFAs. RFAs on JET, for example, have to deal with extremely high heat flux, so design parameters and materials must be chosen accordingly [13].

2.2 Review of Ion Temperature Measurement Methods

2.2.1 Katsumata Probe

The Katsumata probe [14] uses the difference between ion and electron Larmor radii to separate electron and ion currents. Figure 2.1 shows the basic idea of how this difference is exploited [15]. Electrons, with a much smaller Larmor radius, are blocked by a guard electrode. Ions, because of the larger Larmor radius, are able to be measured by the ion collector. The Katsumata probe bias is scanned to measure the ion velocity distribution and allow interpretation of an ion temperature.

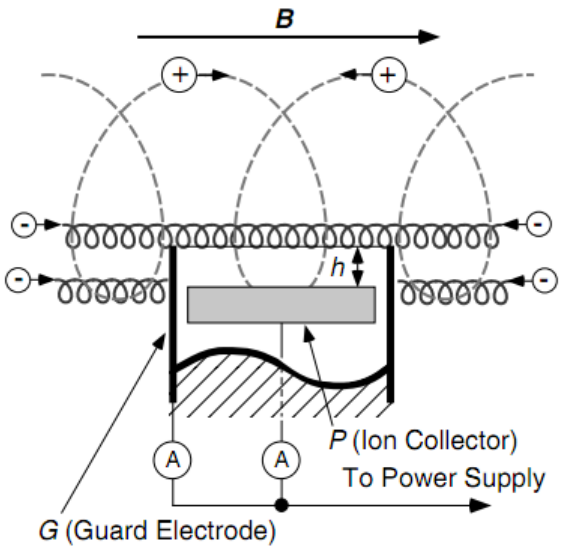

Figure 2.1: Diagram of method of current separation employed by the Katsumata probe.

Interpretation of measurements are difficult with the Katsumata probe, in part because it measures the perpendicular energy, whereas the RFA and other probes analyze the parallel component. For example, it is not clear what happens to the ion distribution when the electrons are simply removed from the plasma [16]. On at least one experiment, RFA and Katsumata probe measurements were substantially out of agreement with each other [16].

2.2.2 Symmetric and Asymmetric Double Probe

The JFT-2M tokamak has employed both the asymmetric and the symmetric double probes in order to measure ion temperature in the edge region of a tokamak plasma [17]. As can be seen in Fig. 2.2, both probes are similar to each other in that they are both double probes mounted on a Macor rod whose axis is perpendicular to the magnetic field [17]. And, in both cases, the rod itself can rotate on an axis perpendicular to the magnetic field.

For the symmetric probe, the head must rotate continuously to get a measurement of ion temperature. As it rotates, one probe will shadow the other one. In this shadow region, only ions with a finite temperature can be measured. By using Monte Carlo simulations to interpret the ion saturation current against the rotation angle, an ion temperature can be calculated [17].

Instead of relying on the rotation angle for temperature calculation, the asymmetric probe

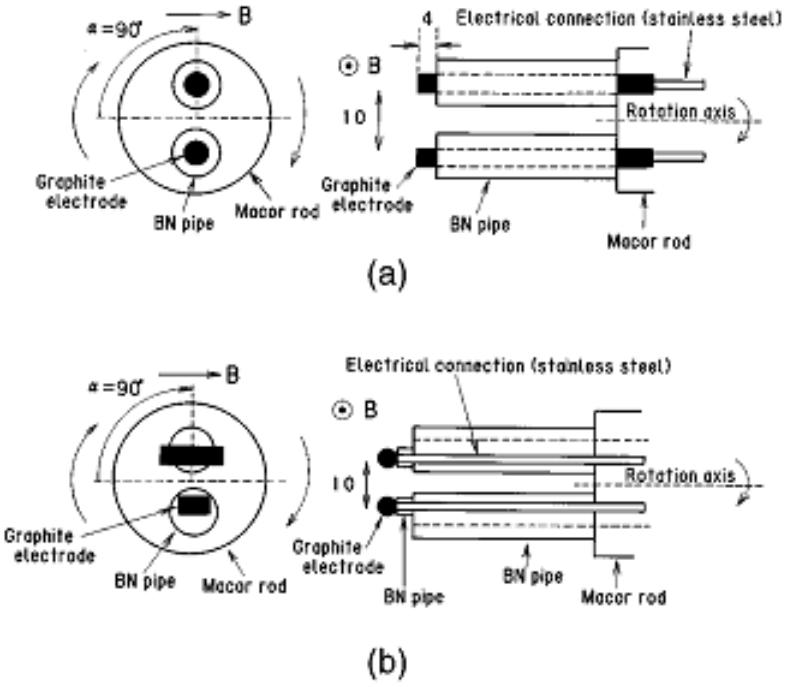

Figure 2.2: (a) Top and side views of the symmetric double probe. (b) Top and side views of the asymmetric double probe.

uses the difference in probe sizes. The ion saturation current reaches a minimum when the axis of the probe electrode becomes parallel with the magnetic field. One electrode being longer, however, it still collects a larger current. The ratio of the ion saturation currents between the two probes is used to calculate the ion temperature [17].

2.2.3 RFA Principles

The RFA is a probe capable of measuring either the electron or the ion temperature. It consists of an entry aperture, several biased grids and a charge collector. Since the electron temperature is easily retrieved from a simple Langmuir probe, RFAs are usually run in ion mode. One of its main advantages is the ease of interpreting temperature.

Fig. 2.3 shows an example of an RFA operated in the ion mode [13]. The entrance aperture is negatively biased with respect to the plasma in order to repel incoming electrons. The first grid is scanned to selectively reject ions, allowing ions with energies above a certain threshold to pass. The second grid is usually the most negatively biased in order to reject the high energy

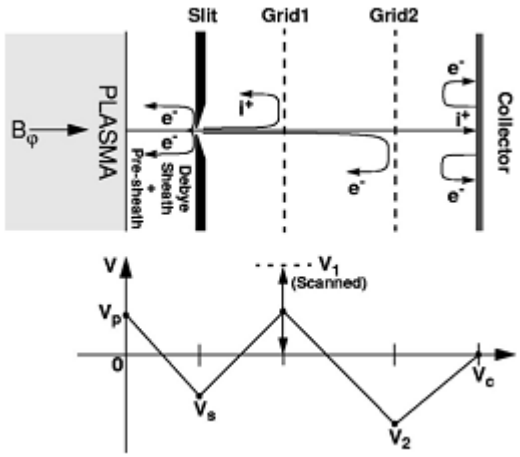

Figure 2.3: TOP: RFA grids BOTTOM: Grid voltages for ion-mode

electrons which overcome the entrance potential and any secondary electrons created on grid 1. Since secondary electrons are also created at the collector, to prevent them from affecting the measured current, this negatively biased grid also ensures these are reflected back to the collector.

The starting place in a derivation of RFA theory is the assumption that the ions maintain a Maxwellian velocity distribution up to the probe surface - in fact, even the idea of a temperature is defined based on the width of a Maxwellian distribution. It is clear that at a higher grid 2 voltage, more ions will be rejected and a lower current will be measured at the collector than when the grid 2 voltage is lower. By measuring particle flux, or current, as the retarding voltage on grid 2 is changed, one can essentially recreate the distribution. Assuming the true distribution to be Maxwellian, one can then determine a temperature, which is defined based on the width of the distribution. This can be simplified to a single relationship between incoming ion current I_i and retarding (scanned) voltage, V.

$$I_i(V) = \begin{cases} I_{0i} & V \leq V_{shift} \\ I_{0i} \exp\left(-\frac{q_i(V-V_{shift})}{kT_i}\right) & V > V_{shift} \end{cases} \tag{2.3}$$

where I_{0i} is the ion current when no ions are repelled and V_{shift} is the potential difference between the plasma and the entrance aperture. Total current is the sum of both ion and electron current, but when the entrance is biased sufficiently negative, the electron current is negligible, so $I_i \approx I_{total}$. For $V > V_{shift}$, if one makes a log plot of the I-V curve, the negative slope is

q_i/kT_i. The retarding voltage is usually scanned between V_{shift} and a value significantly higher than the ion temperature.

When placed within a magnetic field, it is assumed that the axis of the RFA, and therefore its electric field, is aligned with the magnetic field in which it is placed. Only the velocity along the RFA axis is measured, therefore the RFA only determines the parallel temperature. For the sake of simplicity, it is assumed that the parallel and the perpendicular ion temperatures are the same.

In actual use, the temperatures reported by RFA measurements are influenced by the plasma flow [9]. If the plasma flow is known (usually through a Mach probe), then an accurate temperature can be determined from a single sided RFA [18]. However, if a double sided RFA is used, there is no need for a Mach probe. Reference [9] shows how, on a tokamak edge plasma, a simple average of the upstream and downstream temperatures from a double sided RFA provides a very good approximation to the actual plasma temperature, provided the plasma flow speed is not too high. This will be discussed further in Section 5.2.2.

CHAPTER 3

THE EXPERIMENTAL SETUP

3.1 The RFA

3.1.1 Introduction

Before beginning the actual design process, a series of general design parameters was compiled. Firstly, the probe had to be bi-directional. While it is possible to get the temperature with a mono-directional probe in conjunction with a Mach probe [18], bi-directionality provides some advantages. Given that it requires two separate probes, there could be variation of the measured values at their respective locations. Also, requiring a single port is beneficial, especially when working on a large tokamak. It allows the experiment to be more easily implemented.

On some other RFAs (notably JET[13] and Tore Supra[19]) the internal grids were specially made. This is often done at a very high cost. To reduce the cost of this experiment, standard transmission electron microscopy (TEM) grids were used instead. Thus, the dimensions of the inner probe were designed to accommodate the use of these grids.

The RFA will regularly be exposed to the high-heat-flux environment of the tokamak plasma, and therefore, must have certain thermal properties. Not only must the material maintain structural integrity, but its geometry must remain stable (for example, expansion of components might affect inter-grid spacing). For these reasons, the probe housing is made with boron nitride and covered with a graphite cap.

When exposed to a plasma, a conducting material, such as the cap, will approach the floating potential of the plasma. However, the probe drive is electrically grounded to the chamber. It was deemed important to have the cap electrically isolated from ground. Since the mount of

the probe was made from stainless steel, this required a non-conducting piece joining the probe to the mount.

Connected with this is the mechanical strain the probe will experience. The discharges of the HL-2A tokamak are 1 second or more, so to limit the probe's exposure to the plasma and to enable it to take deeper measurements, the RFA was mounted on an reciprocating drive. The drive is rapidly plunged into the plasma until the shaft hits a stopper, which exposes the probe to high accelerations. Therefore, it has to be mechanically sound enough to withstand such conditions.

3.1.2 Entrance Slit

One of the most important components of the RFA is the entrance slit [13]. It is responsible for ensuring that the retarding voltage is experienced by all particles incident on the slit plate and protecting the internal components from the high heat flux of the tokamak plasma.

As described in section 1.2.2, when exposed to a plasma, a Debye sheath forms around a conducting material. The theory of the RFA requires that, when working in ion mode, the incoming electrons be rejected. If the entrance slit is too wide, the Debye sheath will not bridge the gap, therefore, neither will the entrance grid potential. As a result, some electrons will leak through the slit because they will not experience the retarding potential. Figure 3.1 demonstrates this idea. The JET RFA [13] relied on an entrance width $\omega = (1 \rightarrow 2\lambda_D)$. For the Debye length of about 20μm in HL-2A, the slit width used here is 40μm.

While some other RFAs use a single round entrance aperture [18, 20] or a single entrance slit [18, 19, 20, 13], it was deemed necessary to increase the signal-to-noise ratio. This design uses 3 long narrow slits which increases the total slit area, thereby increasing the possible current at the collector plates. The material of the entrance plate is tungsten, chosen for its strength and thermal properties. Figure 3.2 shows a diagram of the entrance plate used.

3.1.3 Probe Body

Many elements for this design were used from the RFA built for STOR-M [18]. The probe body itself is constructed from 4 main components: a machinable ceramic head which holds

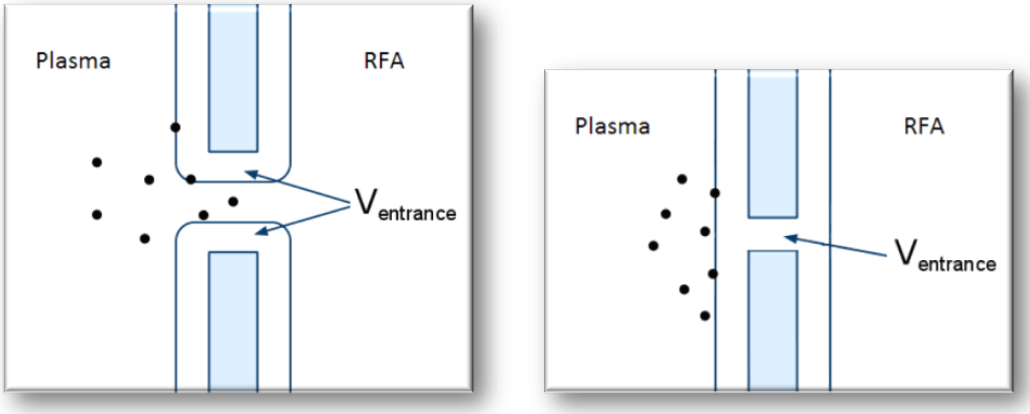

(a) Too wide **(b)** Good width

Figure 3.1: Debye sheath of entrance slit - The black dots represent electrons and the entrance is negatively biased

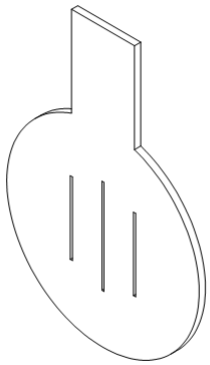

Figure 3.2: RFA Entrance Slit

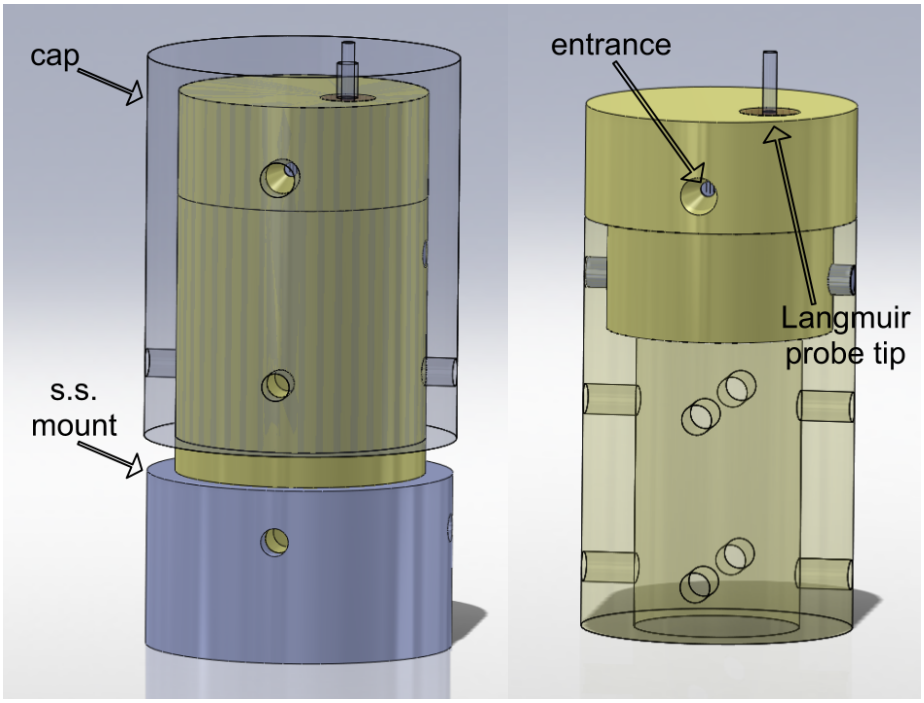

(a) Main probe

(b) Base and head

Figure 3.3: Diagrams of the probe body

the main probe array, a graphite cover which protects the head from plasma heat fluxes, a stainless steel mount which mounts the probe to the probe drive, and a ceramic base which connects the mount to the head. Figure 3.3a shows the probe, with the graphite cover made transparent. Figure 3.3a also shows a Langmuir probe at the top. This was designed and built, but never implemented because it was too far from the entrance slit to provide data of the plasma near the slit. The graphite cover has an outer diameter of 45mm. Without including the mount, the whole probe assembly is 75mm long.

Figure 3.3b shows how the head sits in the base. The head has 2 sections, each with a different radius. It is held in place with a single horizontal pin. The cover is bolted to the base with 4 horizontal holes. The signal wires exit out the bottom of the head and travel through the length of the hollow base, and out through the mount.

A cut-away of the head assembly is shown in Fig. 3.4 where the bi-directionality can be seen clearly. The 2 tapered holes are the upstream and downstream entrances to the probe. The relevant internal components of the head can also be seen clearly in this figure, of which there

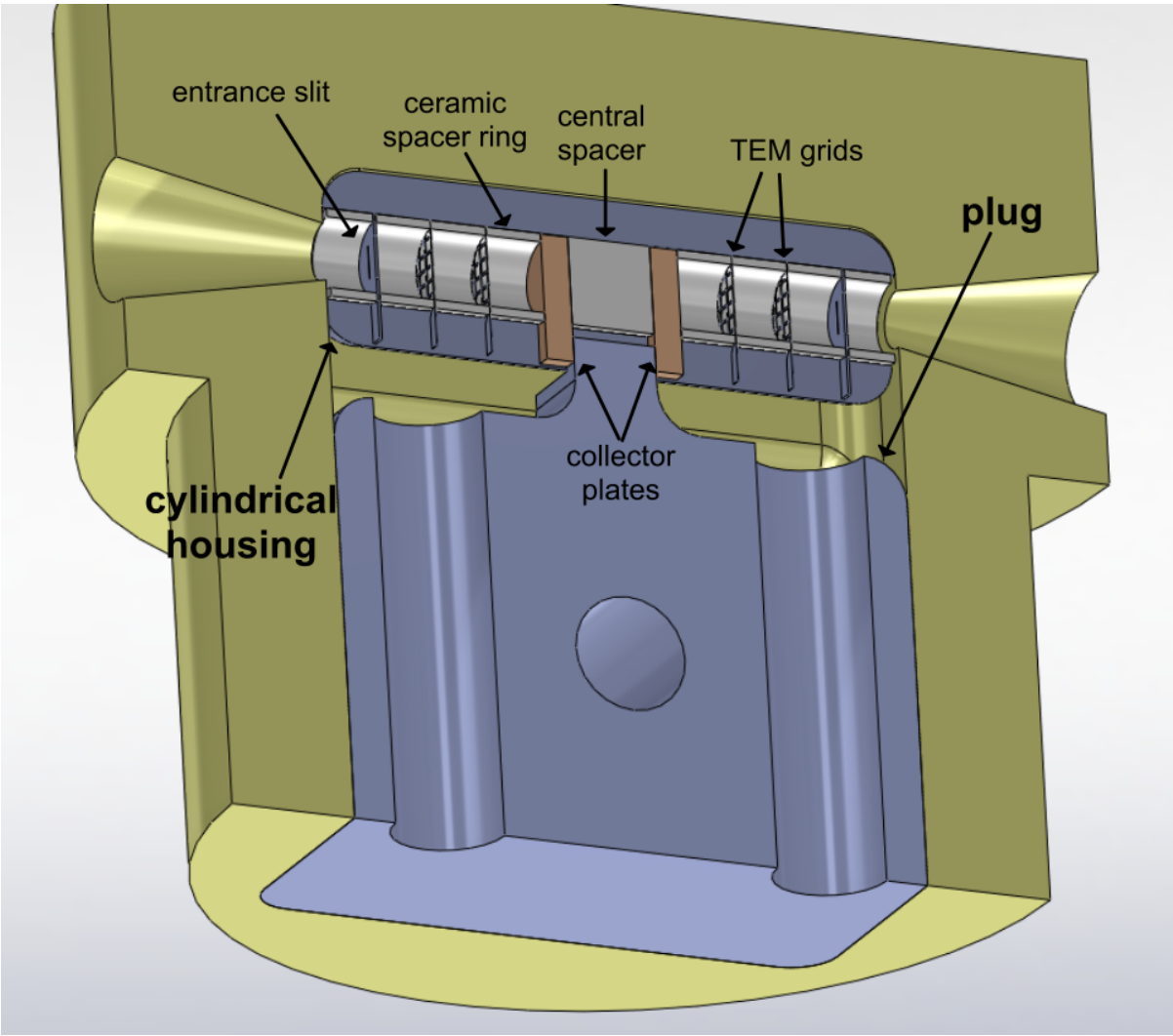

Figure 3.4: Head internals

are 2: the cylindrical piece which houses the probe grid array, and the plug which holds the array in place. The (unused) Langmuir probe is not shown.

The plug, held in place by a single horizontal pin, has two holes, one for each direction, through which pass the signal wires. It is made out of machinable ceramic.

The cylinder, shown in Fig. 3.4, sits in the head and is held in place by the plug. The cylinder holds in place the 2 entrance grids, the 2 collector plates, and the 4 internal TEM grids (2 for each direction). Each side also contain 4 spacers rings, made again of machinable ceramic, which are used to electrically isolate each grid layer from the next. The grid spacing is 2mm, the same used on the JET RFA [13]. In between the 2 collector plates is a central spacer which, unlike the grid spacers, is a solid cylinder. It serves to maintain the independence of both

collector plates. It is also here that the plug compresses and holds the grid assembly. Finally, a thin copper foil was wrapped around the cylinder, careful not to electrically connect any grids, entrance slits, or collectors, to help isolate these components from external EM interference.

3.1.4 Internal Grid Array

TEM grids have a standard external diameter of 3.05mm and a thickness near 35μm. The inner probe is an array of spacers made from machinable ceramic and grids shown also in Fig. 3.4. The inner and outer diameters of the spacer rings is 2.5mm and 3.5mm, respectively.

3.2 Electronics

3.2.1 Data Acquisition

The signals from the probe are carried via coaxial cable to the circuit box, whose schematic is present in Fig. 3.5. The circuit box has 18 used ports (20 in total, but the 2 for the floating probe were not used): 9 inputs and 9 outputs. 8 of the inputs come from the probe: 2 entrance slits (ES A and ES B), 2 scanning grids (G1 A and G1 B), 2 grids for suppression of secondary electrons (G2 A and G2 B), and 2 collector plates (Col A and Col B). The 9th input is the scanning voltage source. Since each input is measured, each is part of a voltage divider, leading to the 9 outputs.

Both entrance grids along with both scanning grids are all biased at a constant DC value. A pack of 22 9V batteries connected in series was used for each of these DC sources (4 packs in total), with points taken at roughly 50V increments. These were connected to a 5 point rotary switch to select the biasing values.

The rest of the circuit box is simply voltage dividers. To monitor the scanning voltage, the signal across a 1/100 voltage divider was measured. The measured signal is V_{G1}mon. To determine the resistors to use on the second grid, it was necessary to estimate the current grid 2 would absorb. The theoretical current on an unbiased entrance grid of diameter 2.5mm is

$$I = \frac{1}{4}An\bar{v}e = \frac{1}{4}Anc_s e \tag{3.1}$$

c_s is the sound speed, which is approximated to be 10^5m/s. n, the density, is about 10^{19}m^{-3} which, when multiplied by e is about 1 Cm^{-3}. The current on the entrance grid is therefore about 30mA. The 3 entrance slits are 40μm wide with a total length of 3mm. This will allow about 3mA of current through. Finally, if the grids are about 60% transmitting, the second grid should experience about 1mA of current. Assuming a maximum current of 5mA, using 0.05W resistors, the resistance value of 1kΩ was chosen.

The collector resistors of 8.2kΩ keep the power requirements below the 2W value for a current of 0.61mA. This was deemed sufficient since the JET RFA [13] notes current less than 0.1mA.

Each of the outputs from the circuit box were passed to an isolation amplifier in order to isolate the box grounds, which are grounded to the tokamak chamber, from the data acquisition ground. Finally, since all the cables used were coaxial, the box inputs each had a sheath that had to be grounded. On the probe end they were all connected together, but not grounded. On the box side, a single sheath was grounded to the box, which was in turn grounded to the tokamak. In this way, ground loops were avoided.

Initial data shows a lot of pick-up noise. The STOR-M RFA [18] used a dummy cable to provide the ability to numerically remove the noise. That technique was also implemented here. Another smaller box was made with a voltage divider using 8.2kΩ resistors, as on the collectors. This signal was measured through the same type of isolation amplifier and was used to numerically remove much of the pick-up noise after measurement.

3.2.2 Scanning Voltage Source

Two different scanning voltage sources were used. The first was a prebuilt 500Hz bipolar source. The scanning range is adjustable from 0 to $\pm$400V and provides ground isolation from a 3-phase wall source.

Preliminary data showed that the high scanning frequency and the negative scanning had an adverse impact on data quality. Therefore, a slower 50Hz unipolar source was built. Figure 3.6 is a picture of the actual setup showing the 2 transformers. The schematic, Fig. 3.7, shows how the transformers are arranged. A variable autotransformer plugged into the wall power source provides an AC voltage source at an adjustable amplitude. The step-up isolation transformer

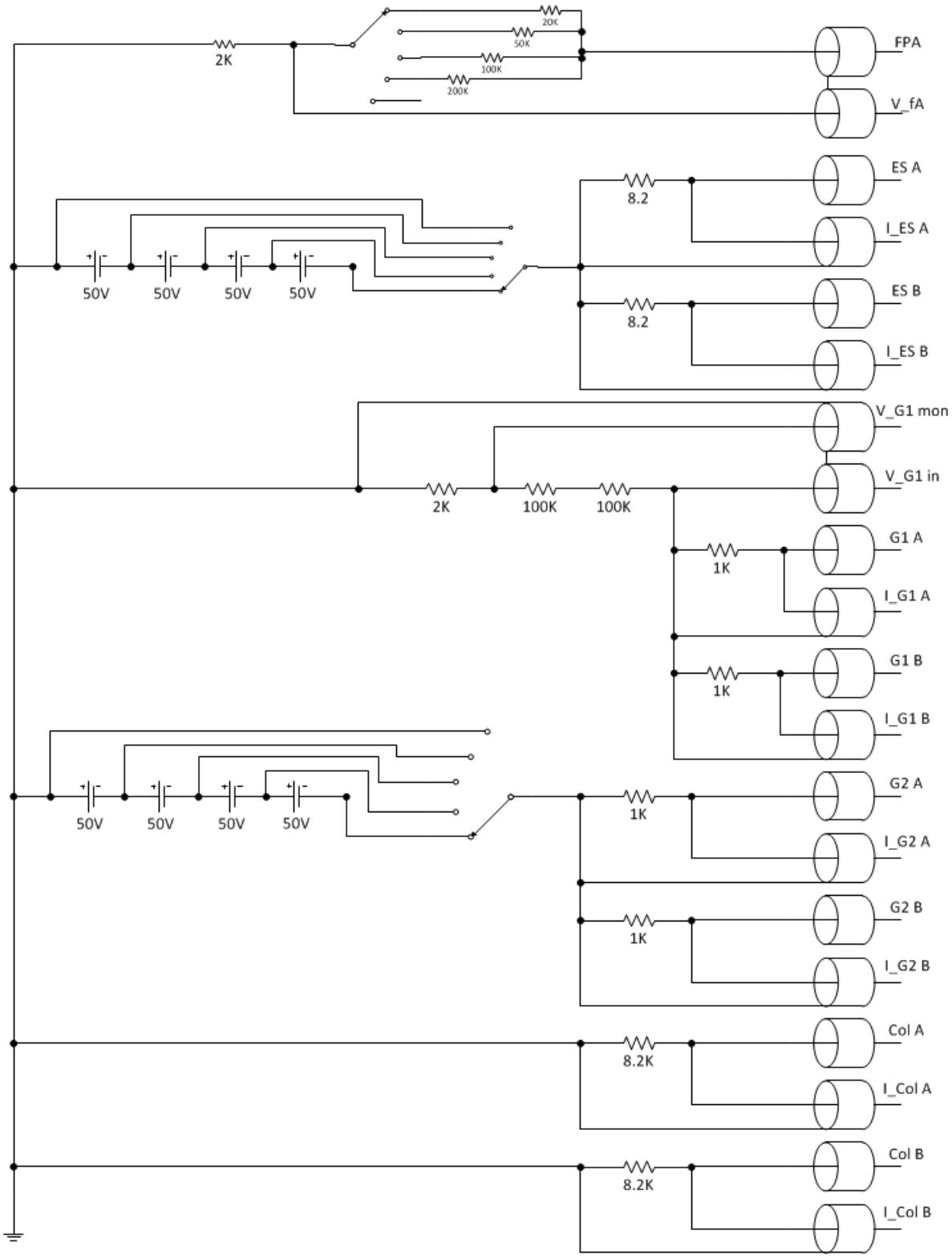

Figure 3.5: Electrical schematic of probe circuitry

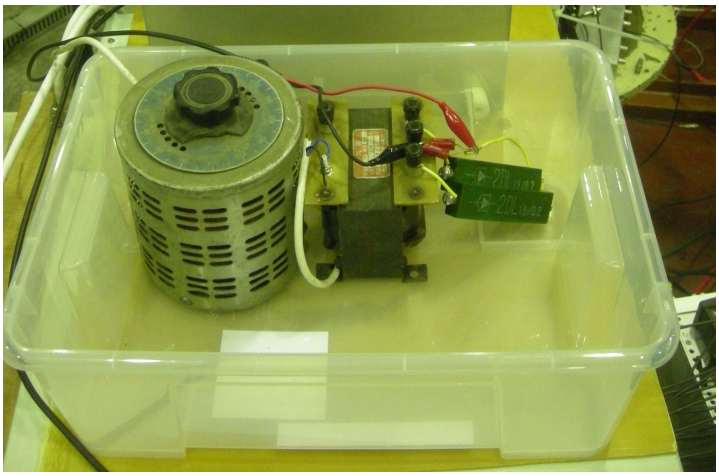

Figure 3.6: The 50Hz scanning voltage source

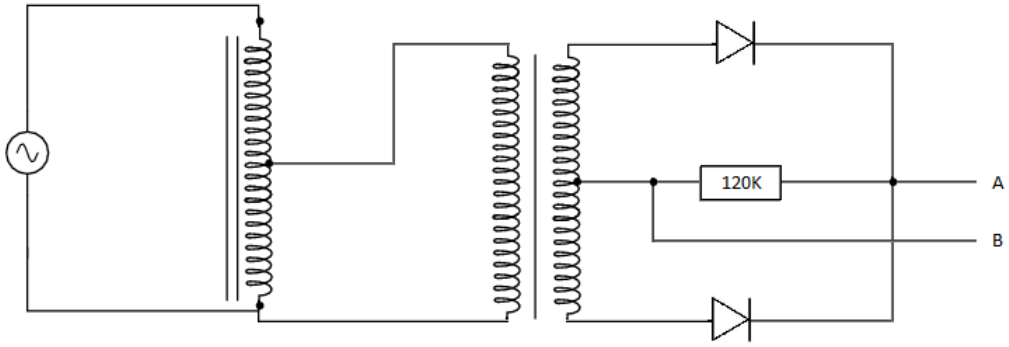

Figure 3.7: Electrical schematic of the 50Hz source

isolates the ground. It has a center pin, which is the output ground reference. The 2 diodes rectify the bi-polar waveform to positive mono-polar scans at 100Hz. While the waveform produced was not triangular, like on JET [13], what is important is the scanning range and frequency. I is a function of V, not the waveform.

3.3 Reciprocating Drive and Tokamak Interface

The probe was mounted on a reciprocating drive. A photo of the drive used can be seen in Fig. 3.8. Figure 3.9 shows a typical plot of the relative probe position with time. Before each shot, the probe is reset to a starting point. During the shot, the probe is triggered and extends 8cm into the plasma in under 0.1s. It stays for a preset time (in the hundreds of milliseconds, controlled

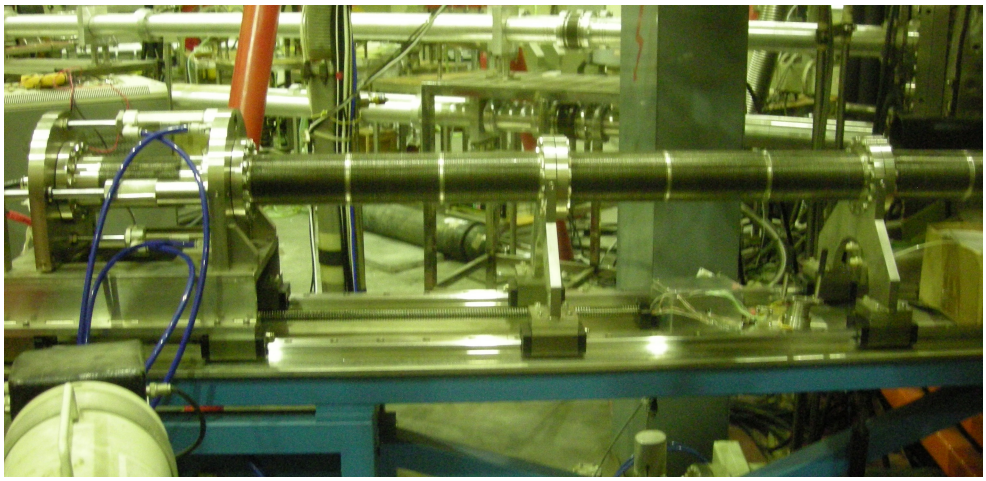

Figure 3.8: Photo of reciprocating drive used on HL-2A

by the experimenter) and retracts. The high acceleration values, above 100g, required that the probe was sufficiently robust.

The drive is used to limit the time the probe is in contact with the plasma, both to protect the probe and to limit the adverse affects on the plasma from the probe. Its most unique advantage, however, is that it also allows the measuring of several temperatures over several centimeters from a single shot, being reconstructed to form a temperature profile. In section 5, data from this experiment will be presented. The details will be discussed there, but one temperature profile is assembled from a single shot, which was only possible because of the reciprocating drive. Another profile is assembled from several shots, each shot providing a single data point from its maximum depth. Because it does not use this last advantage of the reciprocating drive, it provides less meaningful diagnostic information.

3.4 Design Improvements

After review and use of the RFA design described in sec. 3.1, a few issues were identified where improvements could be made. The original goal for this research was to take measurements on the superconducting EAST tokamak, but the timing for the experimental campaign did not work out with when the probe was completed. A redesign, seen in Fig. 3.10, was made to take advantage of both the next campaign and experience gained in making the first probe. This improved design was machined and assembled and is currently in China ready to be

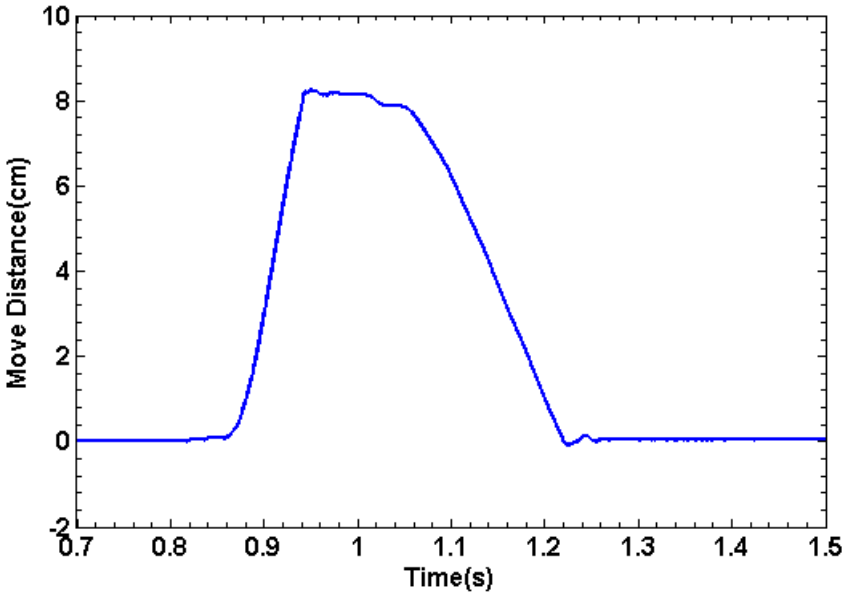

Figure 3.9: Graph of relative position vs time for reciprocating drive. Speed is approximately 1 m/s and the maximum acceleration is above 100G.

implemented on EAST in their 2011 campaign.

The first improvement was the distance the entrance slit sits from top of the probe head. The larger this distance, the deeper the cap must be in the plasma in order to get measurements at a given depth entrance slit depth. This increases the risk and degree of disturbing the plasma and therefore, reduces the potential depth of the probe. In the RFA used for experiments on the HL-2A for this thesis, the center of the entrance slit is 15mm from the top of the cap. The redesign reduces this to 5mm; a significant improvement.

Connected with this was the overall size of the probe head. It was kept circular, partly to give room for the floating probe. Therefore, the width of the probe was determined by the required length of having a bi-directional probe. The width is the main dimension seen by the plasma and is primarily responsible for any perturbations caused by the probe. The outside diameter of the first probe is 45mm. In the redesign, a rectangular shape was adopted which allows the width to be reduced to 13.5mm.

Other more minor improvements were made, including a more mechanically solid structure, improved stabilization of the wiring, and a way to more easily identify the identity of each wire. But the specifics of these details need not be mentioned here. Perhaps when the measurements

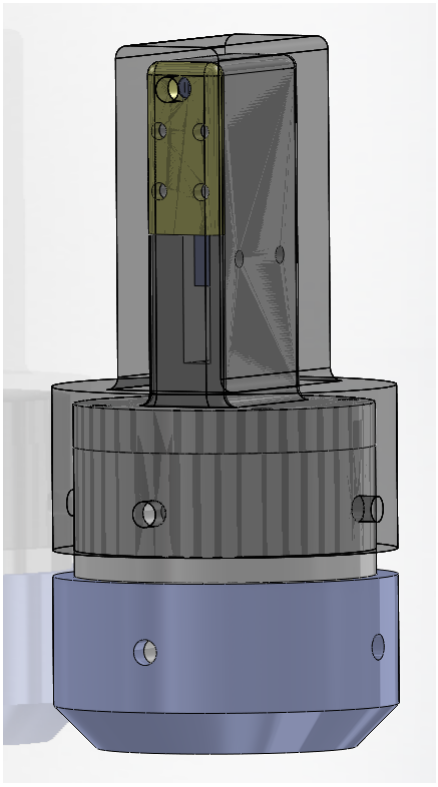

Figure 3.10: The second RFA design. The external graphite cap is made transparent to make the inner parts visible. Note the probe head is no longer circular.

of this newer RFA are obtained and results analyzed, a full description of its design will be presented.

CHAPTER 4

THE MODEL

A model is developed to describe how the measured temperature is affected due to Larmor rotation of the incoming particles. As indicated by eq. 2.3, temperature is found from I, which is a function of scanning voltage V. However, since current is proportional to the particle transmission T, knowing T as a function is V will also provide current, as long as the units are adjusted properly. Therefore, the transmission through the RFA will be derived and used to predict temperature. This derivation is taken in steps, starting with the simplified situation of transmission without particle flow or gate voltage. Then, flow will be introduced. The presence of a gate voltage will be treated separately. Both negative and positive biasing will be considered. For the biased case, essentially the same process will be followed. Where necessary, the evolving description will be compared with known limiting cases. Finally, the positive z direction is defined to be from the probe entrance to the collector, and the r direction is radial from z. As a reminder, the magnetic field is parallel with the z axis of the probe.

From section 2.2.3, the RFA probe is effectively divided into 3 section: entrance to grid 1, grid 1 to grid 2, and grid 2 to collector. Grid 1 is the retarding voltage. The RFA modeled here assumes, for simplicity, no grid 2 and that the scanning voltage is on the collector itself. Essentially, this is modeling the first third of the actual probe. Extensions to the model can be made, but this will still provide an approximation to how temperature is affected by probe geometry.

4.1 General Transmission Function

For a perfectly absorbing surface in a gas, all impinging particles are completely absorbed. All these particles have a net velocity towards the surface; in other words, no particles can hit the

surface from behind. The incident ion flux density Γ_0 (in units of $m^{-2}s^{-1}$) on that surface is calculated by Hutchinson.

$$\Gamma_0 = \frac{1}{4} n \bar{v} \tag{4.1}$$

where n is plasma density and $\bar{v}$ is average particle velocity. To determine T, which is the ratio of transmitted to incident particles, the transmitted ion flux density Γ is calculated. It will then be normalized to Γ_0.

Γ is defined as

$$\Gamma = \int n v_{\parallel} f \mathrm{d}^3\mathrm{v} = n \iiint v_{\parallel} f(v) \mathrm{dv_x dv_y dv_z} \tag{4.2}$$

or in cylindrical coordinates

$$\Gamma = n \iiint v_{\parallel} v_{\perp} f(v) \mathrm{dv_{\perp} dv_{\theta} dv_{\parallel}}. \tag{4.3}$$

The integration variable subscripts $\perp$, $\parallel$, and θ refer to the directions normal to the magnetic field lines, parallel to the magnetic field lines and the azimuthal angle, respectively and $f(v)$ is the distribution function.

The particles in a plasma approximate a Maxwellian distribution function.

$$f = \left(\frac{m}{2\pi kT}\right)^{3/2} \exp\left(-\frac{m(v_{\perp}^2 + v_{\parallel}^2)}{2kT}\right) \tag{4.4}$$

$$= \left(\frac{1}{\pi}\right)^{3/2} \frac{1}{v_{th}^3} \left\{ \exp\left(- \left[\frac{v_{\perp}^2 + v_{\parallel}^2}{v_{th}^2} \right] \right) \right\} \tag{4.5}$$

where m is the ion mass, k is the Boltzmann constant, T is the temperature, and v_{th} is the thermal velocity defined as $\sqrt{2kT/m}$. Simplifying Γ, and seeing that v_{θ} integrates to 2π leads to

$$\Gamma = n \left(\frac{1}{\pi}\right)^{3/2} \frac{1}{v_{th}^3} \left\{ 2\pi \iint v_{\perp} v_{\parallel} \exp\left(-\frac{v_{\perp}^2 + v_{\parallel}^2}{v_{th}^2} \right) \mathrm{dv_{\perp} dv_{\parallel}} \right\}. \tag{4.6}$$

This must be split up into two integrals, Γ_1 and Γ_2, each integrating over parallel and perpendicular velocities. There is more than one way to accomplish this. From Fig. 4.1, it can be seen that all particles with a small enough Larmor orbit will never collide with the cylindrical wall, so all of them should be included in the first integral (blue path in the figure). The remaining ones will have to be moving fast enough so they exit before colliding with the wall (the green path in the figure). Physically, this method works, but another method can simplify the mathematical derivation.

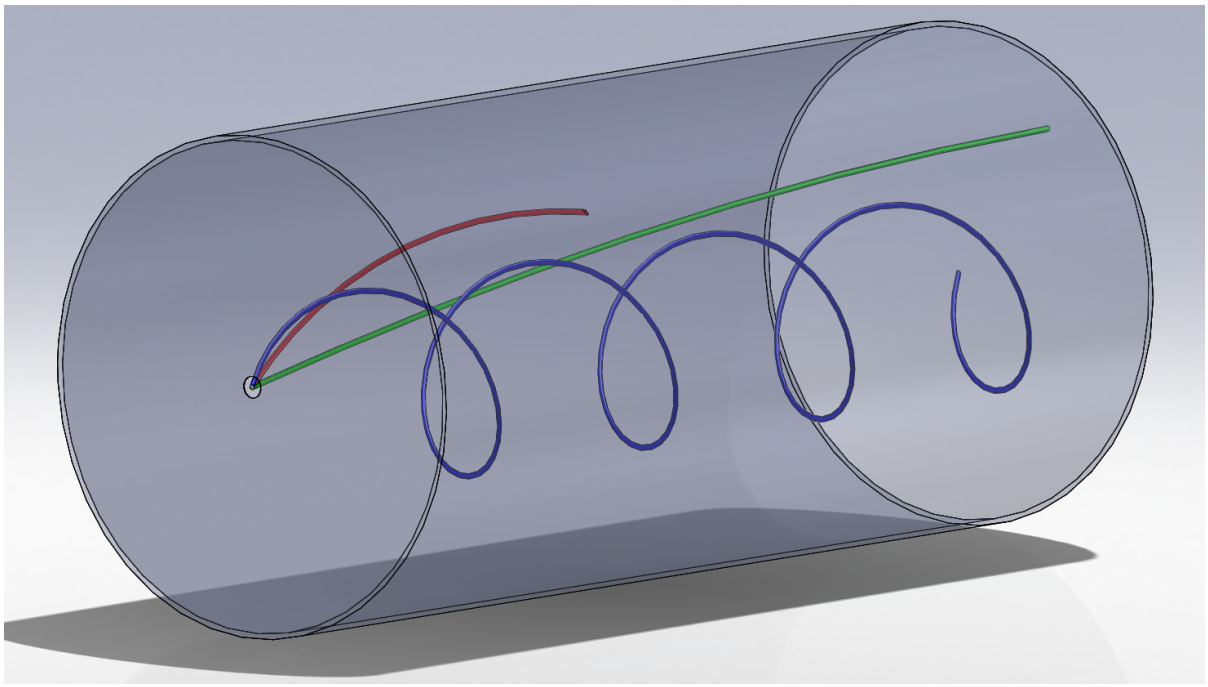

Figure 4.1: A simple graphic showing the different types of particle trajectories possible. Particles all enter the probe at the center of the probe face on the left moving to be collected at the back of the probe (on the right). The retarding voltage source is at the collector. The blue path shows particles whose r_L is small enough that no collisions with the probe wall will occur. $v_{||}$ must only be fast enough to overcome the retarding potential. The red and green paths show particles whose r_L is too large. Only those with a sufficiently high $v_{||}$ (the green path) will traverse the probe. Too slow (red path) and a wall collision will occur. The red path particles will not be detected.

Here, the ions of Γ_1 will all rotate more than π radians during their time in the detector. Therefore, only those ions with a small enough Larmor radius will avoid collision. This will correspond to a limit on $v_\perp$. The ions that rotate less than π radians are counted in Γ_2. Of these, only ions which travel through the RFA before they have time to collide are collected. It will be shown how this also leads to a limit on $v_\perp$. The condition to determine if the particle orbits more or less than π radians will become the $v_\parallel$ limit.

4.2 Non-biasing case

4.2.1 Without Flow

Figure 4.2 shows a cross section of the RFA and an ion's Larmor motion. From the geometry, θ can be found:

$$\sin\frac{\theta}{2} = \frac{a}{2r_L} \tag{4.7}$$

$$\theta = 2\sin^{-1}\left(\frac{a}{2r_L}\right) \tag{4.8}$$

The particle's Larmor radius is given by:

$$r_L = \frac{mv_\perp}{eB} = \frac{v_\perp}{\omega_c} \tag{4.9}$$

where $\omega_c = eB/m$ and is the angular velocity of the particles Larmor rotation, also termed the *cyclotron frequency*.

The time to cross the detector length and the time to cover the arc length are, respectively:

$$t_\parallel = \frac{l}{v_\parallel}, t_\theta = \frac{\theta}{\omega_c} = \frac{2}{\omega_c}\sin^{-1}\left(\frac{a}{2r_L}\right) \tag{4.10}$$

t_θ can be thought of as the collision time. Also, note that θ is limited. If the particle does not collide with the RFA within half an orbit, it will not collide at all. Therefore, $\theta < \pi$. This condition will be used later. Continuing, there are 2 requirements for the particle to pass through the detector.

The first condition is if the Larmor radius is too small to hit the wall,

$$r_L = \frac{v_\perp}{\omega_c} < \frac{a}{2} \tag{4.11}$$

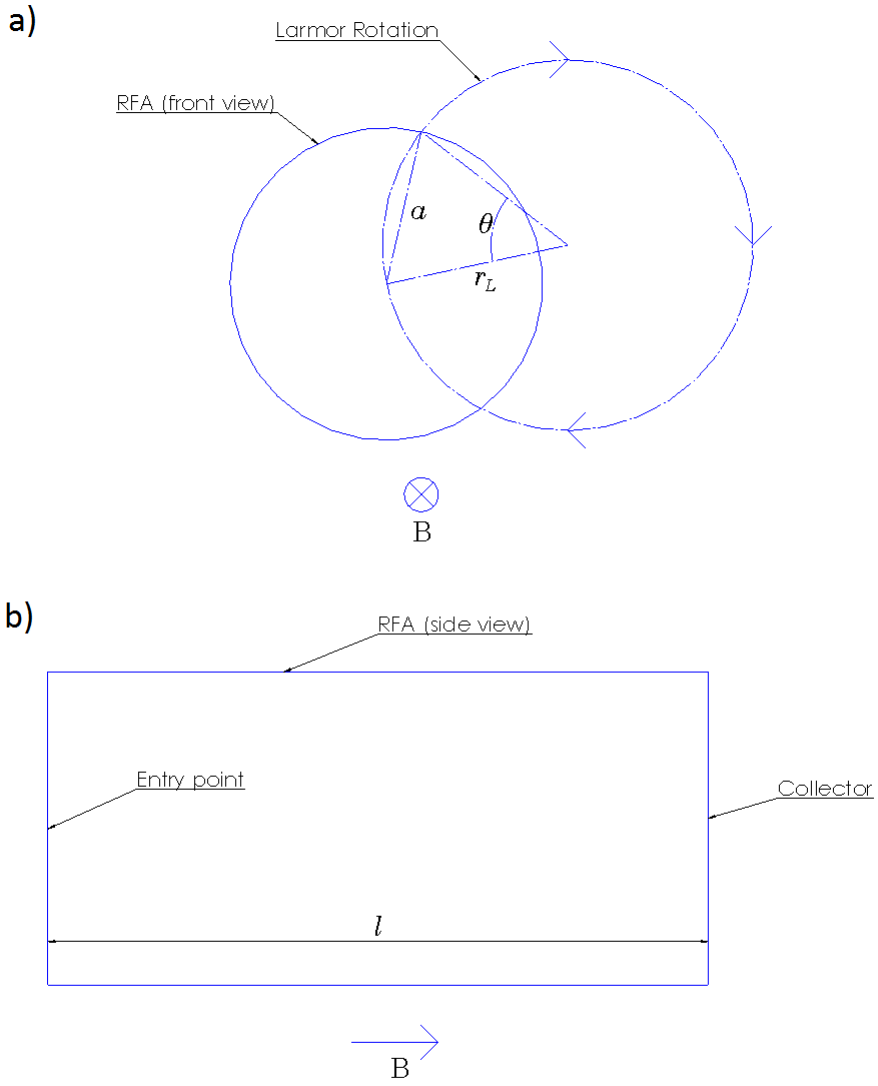

Figure 4.2: a) The modeled RFA from the front. a is the radius of the probe. Particles enter at the center of the plate facing the $\vec{B}$ field. Ions will orbit in this plane according to its Larmor radius r_L. If $2r_L > a$, the particle might collide with the cylindrical wall. The angle through which the particle orbits before collision is θ. b) The same RFA viewed from the side. Particle motion is along $\vec{B}$. l is the length from the entry to the retarding voltage source. The model assumes that the voltage source is at the same position as the collector.

leading to

$$v_\perp < \frac{a}{2}\omega_c \equiv v_{\perp c} \tag{4.12}$$

where $v_{\perp c}$ is defined as the critical perpendicular velocity. This velocity can also be written as:

$$v_{\perp c} = v_{th}\frac{a}{2r_{Lth}} = Rv_{th} \tag{4.13}$$

where $R \equiv a/2r_Lth$ is the internal detector radius normalized to the Larmor radius r_{Lth} for a particle with $v_\perp = v_{th}$.

$$v_{th} = \left(\frac{2kT}{m}\right)^{1/2}, r_{Lth} = \frac{v_{th}}{\omega_c} \tag{4.14}$$

Physically, this is the maximum perpendicular velocity that will fit in the RFA chamber. However, even if the particle moves faster than $v_{\perp c}$, under certain conditions it can still avoid hitting the chamber. This brings us to the next condition.

For all particles with a large enough Larmor radius, they will still avoid the wall if they are collected before collision. Since this inequality contains both $v_\parallel$ and $v_\perp$, either one can be solved for. The 1st case is a critical perpendicular velocity, so another critical perpendicular velocity is defined for this 2nd case using definitions of $t_\parallel$ and t_θ from eq. 4.10, and simplifying with eq. 4.9

$$t_\parallel < t_\theta \tag{4.15}$$

$$\frac{l}{v_\parallel} < \frac{2}{\omega_c}\sin^{-1}\left(\frac{a}{2r_L}\right) = \frac{2}{\omega_c}\sin^{-1}\left(\frac{a}{2}\frac{\omega_c}{v_\perp}\right) \tag{4.16}$$

$$v_\perp < Rv_{th}\left\{\sin\left(\frac{Lv_{th}}{v_\parallel}\right)\right\}^{-1} = g(v_\parallel) \tag{4.17}$$

where $L \equiv l/2r_{Lth}$ is defined as the insulator length normalized to the thermal Larmor diameter. Of course, this is only valid for $v_\parallel > 0$.

In physical terms, this limit corresponds to a limit on the Larmor radius. A lower $v_\perp$ means a smaller r_L, which means that to collide with the wall, the ion must rotate through a greater part of its circular path. Since ω_c is not influenced by $v_\perp$, this means it takes more time to hit the wall.

At this point, the condition $\theta < \pi$ can be combined with eq. 4.16.

$$\frac{\theta}{\omega_c} < \frac{\pi}{\omega_c} \tag{4.18}$$

$$t_{\parallel} < t_{\theta} < \frac{\pi}{\omega_c} \tag{4.19}$$

$$\frac{l}{v_{\parallel}} < \frac{\pi}{\omega_c} \tag{4.20}$$

$$v_{\parallel} > \frac{2Lv_{th}}{\pi} \equiv v_{\parallel c} \tag{4.21}$$

This is defined as the critical parallel velocity. Particles going slower than $v_{\parallel c}$ will rotate more than π radians within the RFA.

R and L were defined as dimensionless values. The remaining terms can be redefined in this way to simplify the mathematical expressions.

$$r \equiv \frac{v_{\perp}}{v_{th}}, z \equiv \frac{v_{\parallel}}{v_{th}}, r_c \equiv \frac{v_{\perp c}}{v_{th}} = \frac{a}{2r_{Lth}} = R, z_c \equiv \frac{v_{\parallel c}}{v_{th}} = \frac{2L}{\pi} \tag{4.22}$$

$g(v_{\parallel})$ from eq. 4.17 can then be simplified

$$g(z) \equiv \frac{g(v_{\parallel})}{v_{th}} = \frac{R}{\sin\left(\frac{L}{z}\right)} \tag{4.23}$$

Now, Γ simplifies to

$$\Gamma = n\left(\frac{1}{\pi}\right)^{3/2} v_{th}\left\{2\pi \iint rze^{-\left(r^2+z^2\right)}\mathrm{drdz}\right\} \tag{4.24}$$

Breaking Γ into the above two cases

$$\Gamma = v_{th}\frac{2n}{\sqrt{\pi}}\left\{\int_0^{z_c}\int_0^{r_c} rze^{-\left(r^2+z^2\right)}\mathrm{drdz} + \int_{z_c}^{\infty}\int_0^{g(z)} rze^{-\left(r^2+z^2\right)}\mathrm{drdz}\right\} \tag{4.25}$$

Figure 4.3 shows graphically the significance of each term in this equation. If $\theta > \pi$, the only particles that will traverse the probe and be detected are those with a small enough Larmor radius ($r < r_c$). These are accounted in the first term ("1" in Fig. 4.3).

If $\theta < \pi$, two groups of particles can still be detected: those with small Larmor radii ($r < r_c$), and those that traverse the probe before colliding with the wall ($r < g(z)$, from eq. 4.17). In the second term, $z \geq z_c$. Given eq. 4.22, it is clear that $g(z) \geq r_c$. Therefore, term 2 includes both of these particle groups.

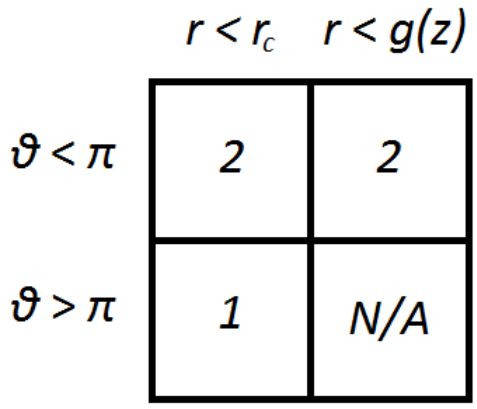

Figure 4.3: A small graphic showing the physical significance of terms 1 and 2 in eq. 4.25. For particle rotations greater than π radians, only one group of particles will be collected: those whose Larmor radius is sufficiently small to fit in the probe (bottom left cell). These are the particles from term 1. For slower rotating particles, 2 groups of particles can make it through: those with small Larmor radii (top left cell) and those fast enough to traverse before colliding with the wall (top right cell). Since $g(z) > r$, term 2 accounts for both of these groups.

In the Maxwellian distribution, if the particles have a net average velocity $\bar{v}$, the whole distribution will be shifted. It is defined by

$$\bar{v} = \sqrt{\frac{8kT}{\pi m}} = \frac{2}{\sqrt{\pi}} v_{th} \tag{4.26}$$

Substituting everything into eq. 4.25 a normalized transmission can be defined.

$$T = \frac{\Gamma}{\Gamma_0} = 4\left\{ \int_0^{z_c}\int_0^{r_c} rze^{-(r^2+z^2)}\mathrm{drdz} + \int_{z_c}^{\infty}\int_0^{g(z)} rze^{-(r^2+z^2)}\mathrm{drdz} \right\} \tag{4.27}$$

The first integral can be solved analytically.

$$T_1 = \left(1-\exp(-r_c^2)\right)\left(1-\exp(-z_c^2)\right) \tag{4.28}$$

The second integral is more complex and retains an integral upon simplification.

$$T_2 = \exp(-z_c^2) - 2\int_{z_c}^{\infty} z\exp\left(-(g(z)^2+z^2)\right)\mathrm{dz} \tag{4.29}$$

A quick check can be done where eq. 4.27 is compared to the limiting case where there is no Larmor motion. This is physically equivalent to making the probe radius infinitely large

with no length.

$$\lim_{R\to\infty} r_c = R \to \infty, \lim_{L\to 0} z_c = 0, \lim_{L\to 0} g(z) = \infty \tag{4.30}$$

In this limiting case,

$$T_1 = 0 \tag{4.31}$$

$$T_2 = 4\int_0^\infty\int_0^\infty rz\exp\left(-(r^2+z^2)\right)\mathrm{drdz} \tag{4.32}$$

$$T_2 = 4\left[\frac{1}{2}\left(1-\exp(-r^2)\right)\right]_0^\infty\left[\frac{1}{2}\left(1-\exp(-z^2)\right)\right]_0^\infty = 1 \tag{4.33}$$

This is the same as saying that $\Gamma = \Gamma_0$, as expected.

4.2.2 With Flow

When there is a positive parallel flow velocity, v_0, the distribution function of the incoming particles can be easily modified. The axis of the probe is parallel with the $\vec{B}$ field and since perpendicular motion is restricted, flow should only appear in the parallel velocity term.

$$f = n\left(\frac{1}{\pi}\right)^{3/2}\frac{1}{v_{th}^3}\exp\left(-\frac{v_\perp^2+(v_\parallel-v_0)^2}{v_{th}^2}\right) \tag{4.34}$$

The normalized transmission is re-written as

$$T = 4\left\{\int_0^{z_c}\int_0^{r_c} rze^{-\left(r^2+(z-z_0)^2\right)}\mathrm{drdz} + \int_{z_c}^{\infty}\int_0^{g(z)} rze^{-\left(r^2+(z-z_0)^2\right)}\mathrm{drdz}\right\} = T_1 + T_2 \tag{4.35}$$

where $z_0 = v_0/v_{th}$. This form is largely unchanged for positive and negative biasing.

4.3 Biasing case

Nearly the same steps will be performed as above but with a potential applied across the detector length from the start. It is assumed that the particles are positive ions with charge e.

4.3.1 Biased RFA in a plasma without flow

The only quantity changed by the voltage will be the parallel velocity, and therefore, the time to cross the detector. Assuming a uniform electric field created by a bias voltage V relative to the entrance aperture, the particle acceleration is found by simple force balancing. The net force F on a particle in flight is due to the electric field, E.

$$F = ma_E = eE = -\frac{eV}{l} \Rightarrow a_E = -\frac{eV}{ml} \tag{4.36}$$

where l is the RFA length, and m is particle mass. Particles moving towards the biased collector are defined to be moving in the positive z direction. Acceleration due to the applied potential a_E is negative because a positive potential will slow the particles down.

The time to cross the RFA, $t_\parallel$, is found using kinematics.

$$l = v_\parallel t_\parallel^2 + \frac{1}{2} a_E t_\parallel^2 \tag{4.37}$$

$$t_\parallel^2 - \frac{2mlv_\parallel}{eV} t_\parallel + \frac{2ml^2}{eV} = 0 \tag{4.38}$$

$$t_\parallel = \frac{l}{eV}\left(mv_\parallel \pm \sqrt{(mv_\parallel)^2 - 2meV}\right) \tag{4.39}$$

This derivation should hold both for positive and negative potentials (though, not for $V = 0$). If the applied potential is negative, the positive option in eq. 4.39 becomes negative, which is not physical. Therefore, the negative option is taken as physically correct.

$$t_\parallel = \frac{l}{eV}\left(mv_\parallel - \sqrt{(mv_\parallel)^2 - 2meV}\right) \tag{4.40}$$

This is the parallel flight time for a particle in a potential barrier, replacing eq. 4.10.

Since the potential only alters motion in the z direction, the first condition is unaffected. The second condition (eq. 4.15), with t_θ unchanged, leads to a new form for the condition on $v_\perp$.

$$v_\perp < \frac{Rv_{th}}{\sin\left(\frac{Lv_{th}(mv_\parallel - \sqrt{(mv_\parallel)^2 - 2emV})}{eV}\right)} = g(v_\parallel) \tag{4.41}$$

Again, to find a condition for $v_\parallel$ the condition above is combined with the limit on θ ($\theta < \pi$ from eq. 4.18). This inequality is difficult to solve analytically because it requires squaring both sides of an inequality. Instead, it is much simpler to approximate a solution for $v_\parallel$ numerically.

As before, the set of dimensionless quantities is defined, beginning with a potential normalized to the thermal kinetic energy.

$$\overline{V} = \frac{eV}{{}^{1}/_{2}mv_{th}^{2}} \tag{4.42}$$

The new normalized velocities follow from this.

$$g(z) \equiv \frac{g(v_{\parallel})}{v_{th}} = \frac{R}{\sin\left(\frac{2L\left(z-\sqrt{z^2-\overline{V}}\right)}{\overline{V}}\right)} \tag{4.43}$$

$$z_c \equiv \frac{v_{\perp c}}{v_{th}} \tag{4.44}$$

All the integration limits have been redefined, but one final quantity needs to be defined before the transmission integrals can be determined. Because of the biasing, it is possible that the ion's kinetic energy is insufficient to be transmitted through the probe. z_s is defined as the minimum normalized ion velocity for detection.

$$\left(\frac{1}{2}mv_{\parallel}^{2} \geq eV\right) \Rightarrow \left(v_{\parallel}^{2} \geq \frac{2eV}{m}\right) \Rightarrow \left(\frac{v_{\parallel}^{2}}{v_{th}^{2}} \geq \frac{eV}{kT}\right) \Rightarrow \left(z^2 \geq \overline{V}\right) \tag{4.45}$$

$$z_s \equiv \begin{cases} \sqrt{\overline{V}} & \text{if } \overline{V} > 0 \\ 0 & \text{if } \overline{V} \leq 0 \end{cases} \tag{4.46}$$

For values of z_c greater than z_s, the form of the integral is unchanged from the unbiased case, with the exception of z_s, which only appears in the first integral.

$$T = 4\left\{\int_{z_s}^{z_c}\int_{0}^{r_c} rz\exp(-(r^2+z^2))\mathrm{drdz} + \int_{z_c}^{\infty}\int_{0}^{g(z)} rz\exp(-(r^2+z^2))\mathrm{drdz}\right\} \tag{4.47}$$

$$T_1 = \left(1-\exp(-r_c^2)\right)\left(\exp(-z_s^2)-\exp(-z_c^2)\right) \tag{4.48}$$

$$T_2 = \exp(-z_c^2) - 2\int_{z_c}^{\infty} z\exp\left(\left(g(z)^2+z^2\right)\right)\mathrm{dz} \tag{4.49}$$

However, when $z_c \leq z_s$, the biasing is negative, so $z_s = 0$ and $z_c \leq 0$. Physically, this means that even particles with a negligible initial parallel velocity can be accelerated fast enough

through the chamber to avoid the wall. None of the particles in the chamber will orbit under π radians, so the first integral T_1 goes to 0. All particles are taken into account with only T_2. Hence, the whole transmission becomes simply

$$T = 4\int_0^\infty \int_0^{g(z)} rz\exp(-(r^2+z^2))\mathrm{drdz} \tag{4.50}$$

or, simplified

$$T = 1 - 2\int_0^\infty rz\exp\left(-(g(z)^2+z^2)\right)\mathrm{dz} \tag{4.51}$$

4.3.2 Biased RFA in a plasma with flow

When the normalized critical parallel velocity is positive ($z_c > z_s$), introducing flow leads to nearly the same transmission integrals as the unbiased case using the redefined integration limits.

$$T = 4\left\{\int_{z_s}^{z_c}\int_0^{r_c} rz\exp(-(r^2+(z-z_0)^2))\mathrm{drdz} + \int_{z_c}^\infty\int_0^{g(z)} rz\exp(-(r^2+(z-z_0)^2))\mathrm{drdz}\right\} \tag{4.52}$$

$$T_1 = 2(1-\exp(-r_c^2))\int_{z_s}^{z_c} z\exp\left(-(z-z_0)^2\right)\mathrm{dz} \tag{4.53}$$

$$T_2 = 2\int_{z_c}^\infty z\exp\left(-(z-z_0)^2\right)\left(1-\exp(-g(z)^2)\right)\mathrm{dz} \tag{4.54}$$

This case corresponds to particles with an initial velocity into the RFA. When $z_c < z_s$, however, the first integral goes to 0 as described in the flowless case. Again, defining flow velocity by v_0 and normalizing by thermal velocity, $z_0 \equiv v_0/v_{th}$.

$$T = 2\int_0^\infty z\exp\left(-(z-z_0)^2\right)\left(1-\exp(-g(z)^2)\right)\mathrm{dz} \tag{4.55}$$

4.4 Model Predictions

Recall that eq. 2.3 is used to interpret a temperature from I as a function of V. The negative reciprocal of the slope of the $\log(I)$ vs V curve is the measured temperature. I, as the measure of charge per second passing through a defined cross-sectional area, is directly proportional to the particle flux density Γ of eq. 4.6 for the same area, thus, temperature can be interpreted from $\Gamma(V)$. Transmission was defined in eq. 4.27 by normalizing $\Gamma(V)$ to the thermal flux density Γ_0. This means that the negative reciprocal of the slope of the $\log(T)$ vs I curve provides a "thermal" temperature: the interpreted temperature normalized to the actual temperature. An output of 1 means that probe geometry does not affect temperature interpretation. T was determined by numerically solving eqs. 4.53 and 4.54. Matlab was used.

Probe geometry is not the only thing that affects RFA temperature interpretation. An RFA facing plasma flow and one measuring the same plasma but facing away from the flow will both measure different temperatures. Flow is quantified in this case by a *Mach number*, M. It is defined as

$$M = \frac{v_p}{c_s} \tag{4.56}$$

where v_p is the average velocity of the Maxwellian distibution, and c_s is the ion sound speed. The influence of plasma flow is commonly removed by averaging the upstream and the downstream temperature measurements. This practice will be investigated later in this report but for the purposes of demonstrating model predictions, the transmission of the probe facing the plasma flow used a positive Mach number (M_+) with a negative Mach number (M_-) upstream being used for the other probe (where $M_+ = -M_-$). The resulting temperatures were averaged.

Figure 4.4 shows the predictions of the model for Mach numbers from $M = 0$ to $M = 0.3$. The probe dimensions used in Fig. 4.4 were from the current probe with $a = 1.25$mm and $l =$ 2mm. As can be seen from the figure, the model predicts an overestimation of ion temperature. Even when no plasma flow is present, with $T_m = 50$eV, the normalized ion temperature is 5% higher. With a higher Mach number, the discrepancy is increased. With the same measured temperature of 50eV at $M = 0.3$, the reported temperature is 10% higher than the actual.

This model makes the simplifying assumption that the retarding potential sits at the back of the probe. Figure 4.5 shows the normalized measured temperature, T_m/T_i, plotted with

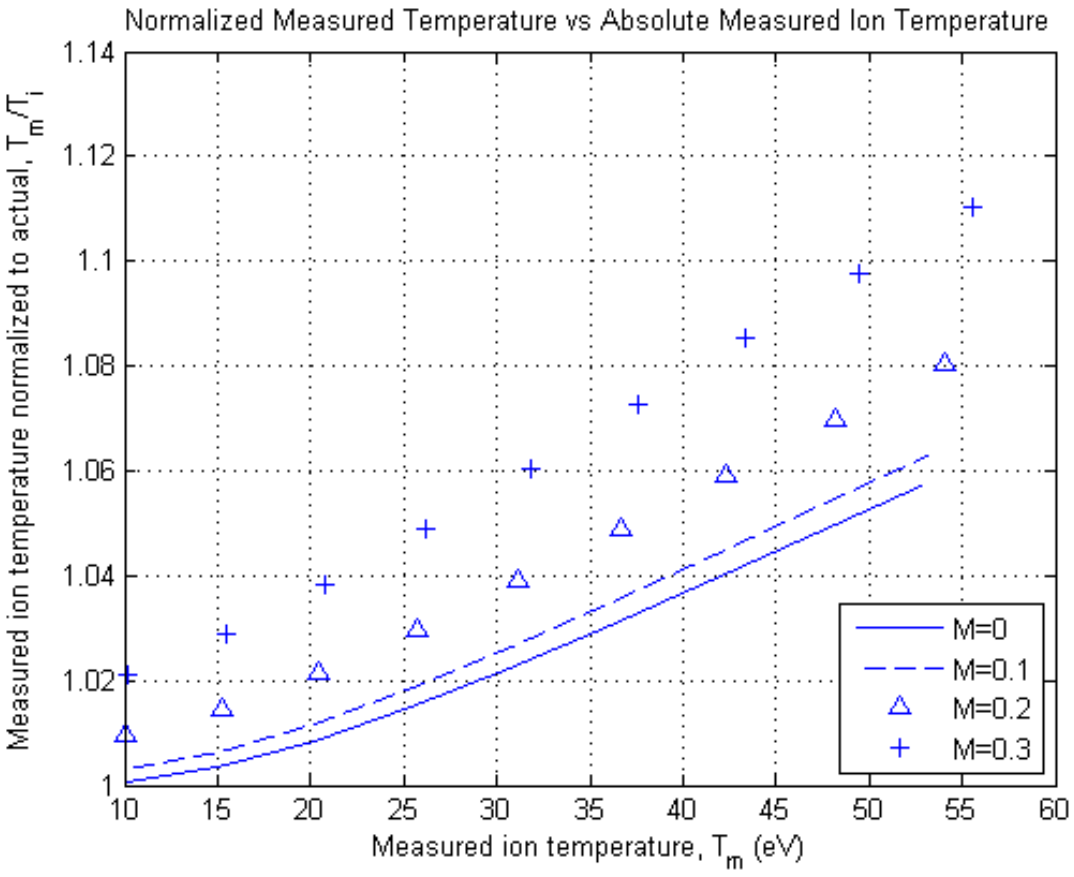

Figure 4.4: Normalized measured ion temperature vs absolute measured temperature for various Mach numbers. Both values are the resulting temperature averaged from the upstream and downstream measurements. $a = 1.25$mm, $l = 2$mm.

respect to probe length, l, from 0.1mm to 6mm. The probe radius used in this simulation is $a = 1.25$mm, the radius of the probe built in this experiment. The plot shows that, for this probe radius, there is a maximum over-estimation of temperature between 1mm and 2mm. This is somewhat surprising. It is not clear precisely why the ratio begins to drop after about 1.5mm. But, it is noticed that at probe lengths larger than about 3mm, effectively the only particles getting through are those whose r_L values fit within the RFA. Very few particles with larger Larmor radii are fast enough to avoid wall collisions. This means that the transmitted 2-D velocity distribution is no longer a function of probe geometry. It should, theoretically, be possible to reconstruct the whole distribution only measuring one of the tails, so it is not necessary to have the whole distribution to measure a temperature. Perhaps the influence of probe geometry on temperature stems from the fact that the transmitted velocity distribution changes with changing l.

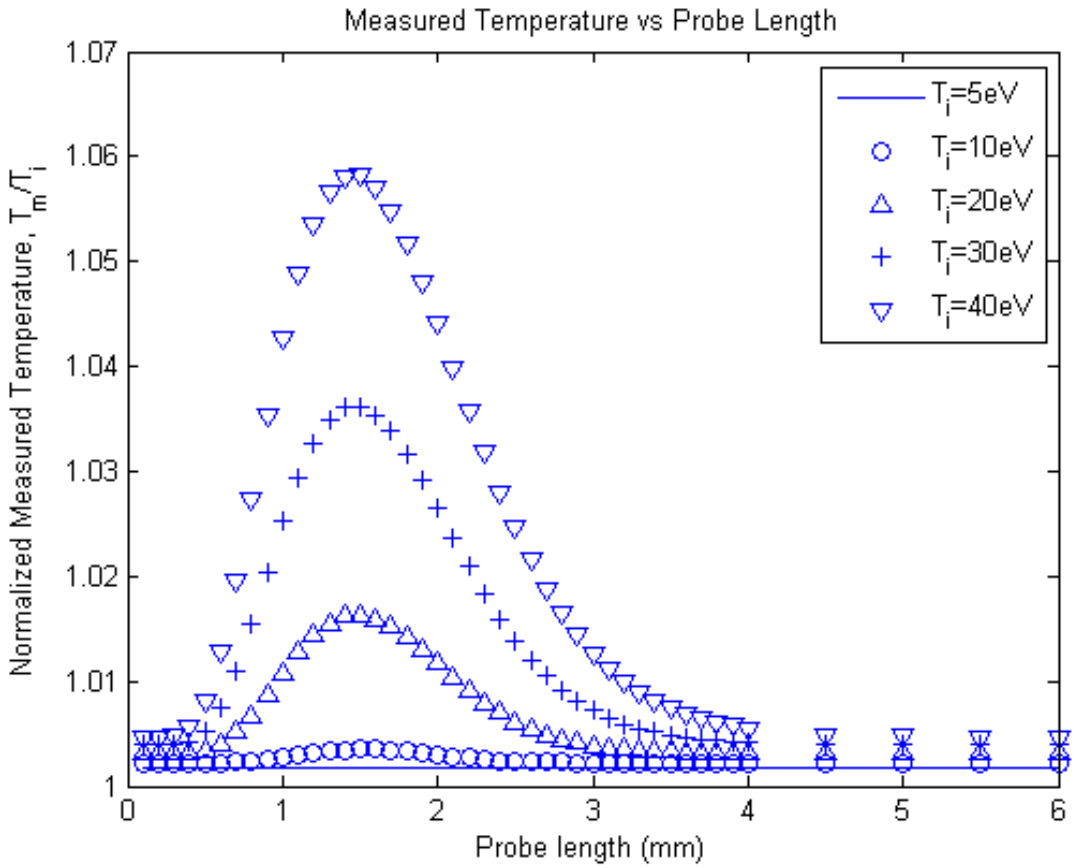

Figure 4.5: Ratio of measured to actual ion temperature vs probe length for various ion temperatures. Probe radius here is $a = 1.25$mm and Mach number is $M = 0.1$.

CHAPTER 5

RESULTS

5.1 Qualitative Analysis

Figure 5.1 shows an example of the data collected from the RFA at HL-2A. As noted earlier, the probe is mounted on a reciprocating drive. The time frame of the figure, indicated by vertical dashed lines, is approximately when the probe is at the maximum depth. The last closed surface of the plasma is at roughly r=38cm so, with the probe at a maximum depth of 42.5cm in this shot, it is still very much in the scrape-off layer.

The bottom plot shows the MHD signal. Where B_p^* is the perturbed component of the poloidal magnetic field, this signal is dB_p^*/dt. It is indicative of the instabilities in the plasma and was plotted because there was a noted correlation on many shots between high MHD activity and the presence of noise in the RFA signals.

The Data Acquisition System (DAQ) provided data at 1MHz which was a much higher temporal accuracy than the experiment as a whole. Therefore, in order to produce smooth graphs, signals were numerically averaged over 1000 points, corresponding to 1ms. Additionally, when the first plots were made, they were seen to be highly affected by external noise, some of which was at the same frequency as the scanning voltage signal. A dummy wire was installed which ran alongside both current signal wires and the scanning voltage wire. It was used to numerically remove the common mode noise from the current signals. This method allowed a reduction of noise of at least an order of magnitude.

While HL-2A offered a very unique opportunity it was not without its difficulties. HL-2A is a much larger tokamak than, for example, STOR-M, and as such, it had many other experiments going at the same time. Due to time and space constraints, the RFA did not get specific experiment time with controlled machine parameters. So long as other experiments

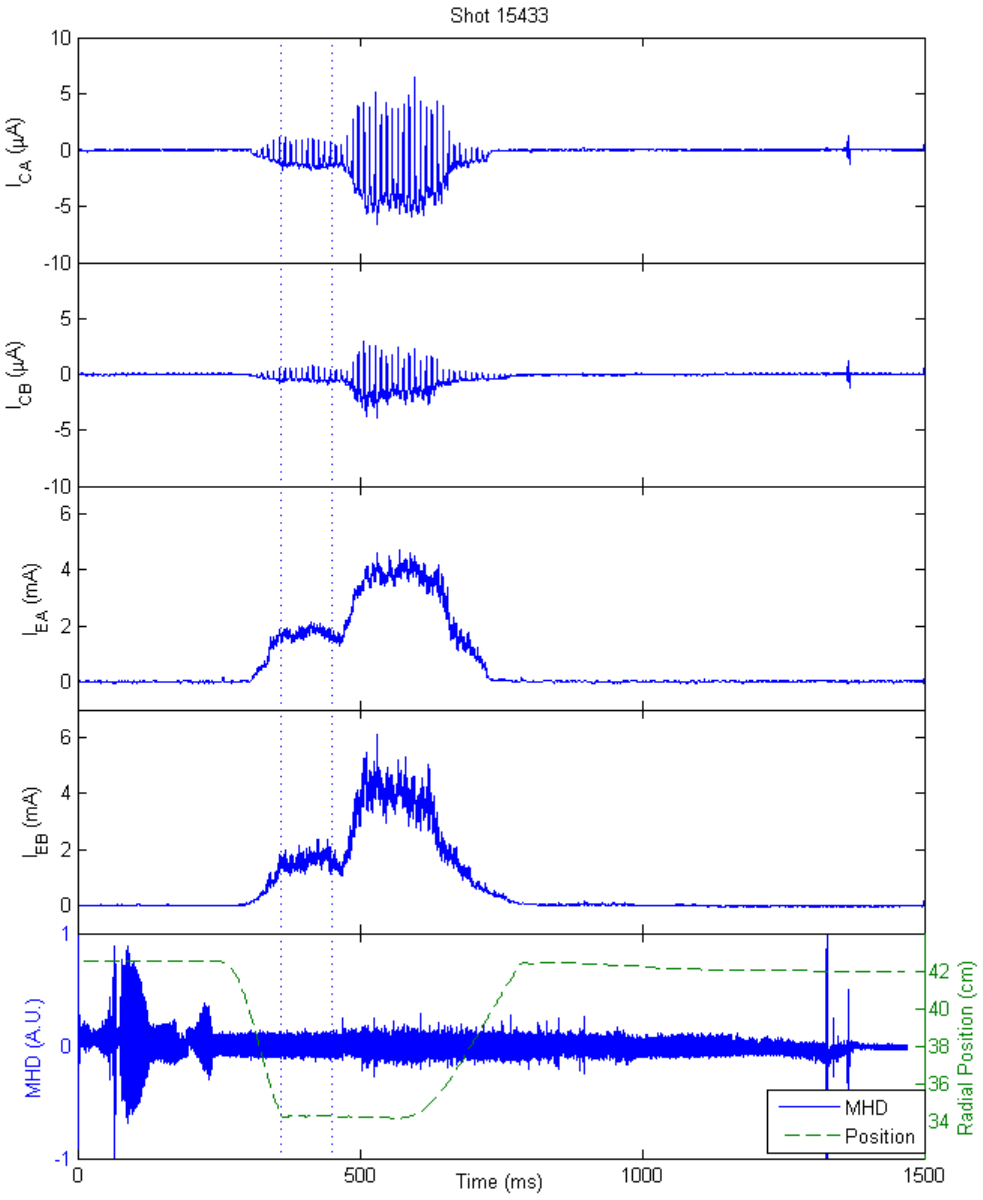

Figure 5.1: Example shot data for shot 15433 on HL-2A. The top 2 plots show collector current for probes A and B. The 2 plots below that show the current measured at the entrance grid for each probe. Finally, the MHD activity is plotted along with the probe position. Arbitrary units are used for the MHD signal. dotted lines indicate the range over which data was analyzed for this shot.

were not adversely affected, RFA measurements could be carried out. This made it impossible to take data close to the plasma edge. Additionally, sometimes machine parameters were not ideal for RFA measurements. Density is a critical issue, discussed in many RFA experiments [18, 20, 13]. MHD activities also can disturb data. Neither of these were controlled for this particular experiment. It was noticed that there was often a correlation between a strong MHD signal and noise in the current measurements. To mitigate this weakness as best as possible, it was important to take measurements on various different shots to find those that were not significantly affected by MHD activities. In shot 15433 (Fig. 5.1), the MHD signal was relatively small and stable and RFA data was less affected.

Figure 5.2, the same data as presented in Fig. 5.1 but expanded to depict important features, shows qualitatively how an RFA measurement is expected to behave. When V_{scan} is at the maximum value (around 200V), both collector currents are at a minimum since most ions are rejected, and as the voltage drops to zero, ions are no longer rejected and both currents spike. It can also be determined that the scanning voltage is sufficiently high since, in between each current peak, the current trace is approximately flat. This indicates that effectively all of the ions are blocked. The ion signal should be positive throughout and the baseline should be 0. Although the exact cause of the apparent DC shift is not completely clear, the drift can be numerically removed for further quantitative analyses. There is also a visible relationship between entrance current and the collector current peaks. When the entrance current suddenly increases at around 500ms in Fig. 5.1, the collector current peaks increase as well. This will be discussed further below.

All of these positive characteristics are also seen in the results from JET, reprinted in Fig. 5.3. One important difference, however, is that the noise level in the collector current traces (the 4th and 5th plots) is much lower. This allows for a higher spatial and temporal accuracy making an ion temperature profile from a single shot much more accessible. The primary benefit of the reciprocating drive is the ability to measure a temperature profile in a single shot, and with the low noise levels of the JET RFA, this is much more readily achievable. Another difference is that they were able to insert the RFA much deeper in the plasma. As mentioned in the previous section, the RFA re-design is intended to address this current weakness. On top of the mechanical redesign of the probe, noise level could be reduced with more attention paid

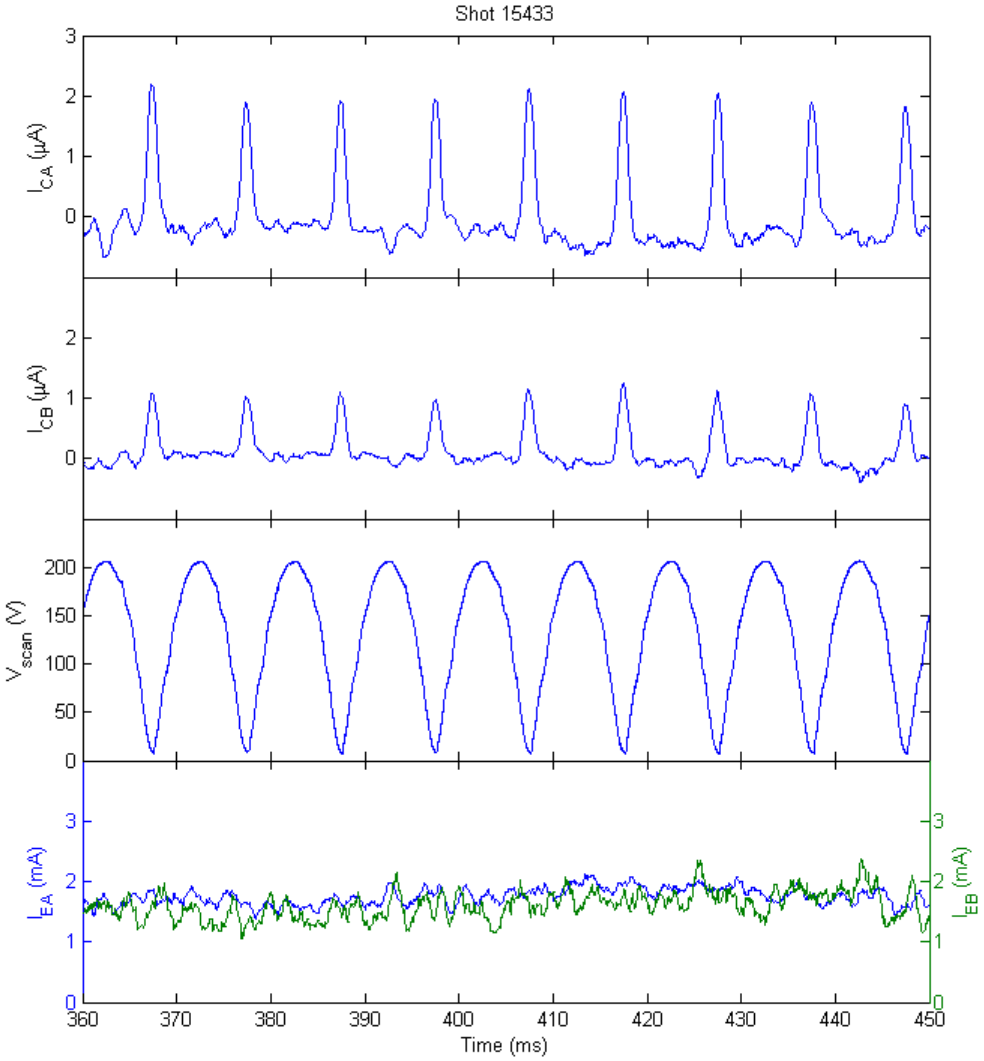

Figure 5.2: Plot of relevant RFA data for time window indicated in Fig. 5.1. At the top is plotted the collector current for each probe. The DC levels stay relatively constant in this time frame and so, have been zeroed. Below that is shown the scanning voltage. Finally, both entrance currents are plotted.

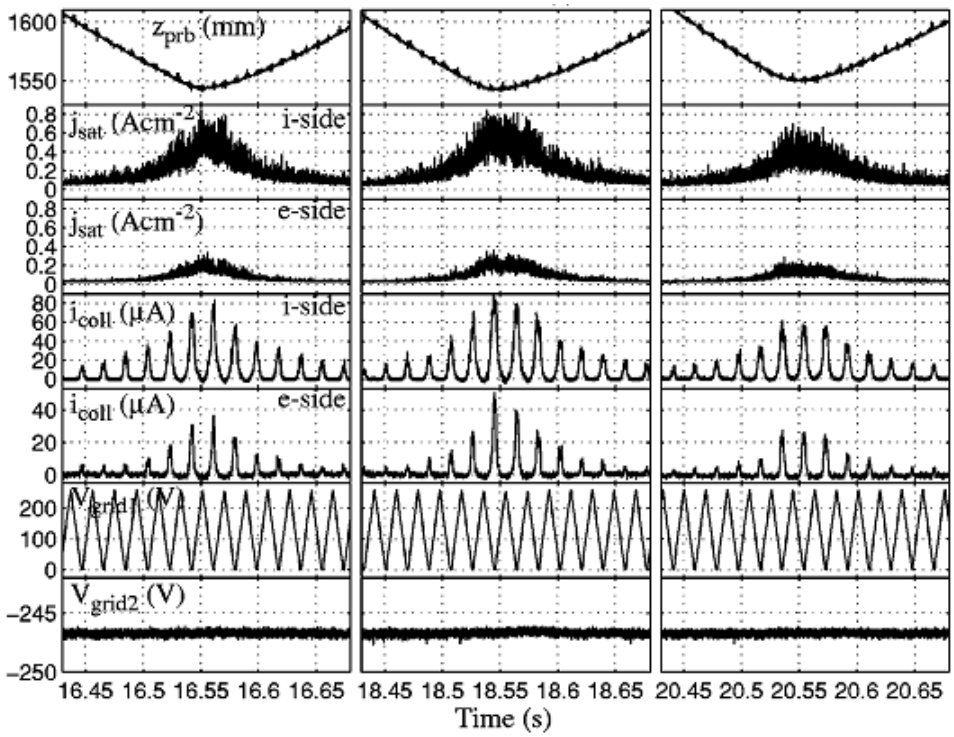

Figure 5.3: Reprinting of JET RFA data [13] to compare qualitatively. The top plots indicate the scanning probe position. As it goes deeper into the plasma, ion-side and electron-side saturation currents correspondingly increase. As well, the peaks of the collector currents increase with decreasing probe position. The scanning potential is next, followed by the voltage of secondary electron repelling grid. Closer examination shows the same inverse relationship between scanning potential and collector current as is shown in Fig. 5.1.

to the electronic circuits.

Figure 5.2 demonstrates that the signal from probe A was stronger. This was noticed in every shot examined. Comparing plots 4 and 5 from Fig. 5.3, it is noticed on the JET RFA that one probe also reports higher current levels, but the stronger signal in JET's data always corresponds to the probe on the ion-side, or, in other words, the upstream probe. As mentioned previously in this report, the positive flow present at the upstream probe will result in a higher temperature than the negative flow of the downstream probe for the same measurement. The prediction that upstream probes measure a higher temperature is born out in the rest of JET RFA article[13]. Examination of the data from the present device shows, however, that regardless of which probe measured the higher temperature, probe A still reported stronger signals. Since qualitative observations in this section agree with theory, and numerical analysis in the

next support previous RFA measurements, this issue is not expected to significantly affect the voltage dependence of current. In other words, the lower signal in probe B does not appear to be a function of ion velocity.

One possibility that was investigated was differences in probe geometry. Once assembled, all components of each probe were fixed. However, during probe assembly some minute variability in probe component placement was observed. This is not expected to be a factor because any change in probe geometry would likely introduce an energy-dependent difference in ion current, resulting in different temperatures, and this is not what was noticed. A more likely possibility is that asymmetries in the circuits from probes A and B cause a higher effective resistance in one side. Potential sources of this difference that can be examined for the next probe could come from the lines within the reciprocating drive itself, resistance added at coaxial connection points, or asymmetries in the circuit control box. Finally, contaminants on any of the grids, collectors, or entrance plates could affect the current measured. Especial care must be paid during probe assembly.

As just mentioned, a reciprocating drive plays a key role in retrieving a profile of ion temperature obtained from a signal shot, one temperature measurement coming from each voltage scan. This has been done successfully on different machines [18, 20, 13]. The deepest insertions done with this probe, however, reported data that was too noisy to obtain confident temperatures for each voltage scan. Therefore, two different profiles will be presented in the next section: one from the single shot 15558, providing a profile between $r \approx 41.2$cm and $r \approx 43$cm and another from a collection of 22 different shots with a deeper profile between $r \approx 39$cm and $r \approx 43$cm. This second profile requires the averaging of several measurements from a single shot.

In order to average the data from a single shot, a time window needs to be chosen over which important quantities are relatively constant. The choice of the time window for analysis was made using entrance current measurements as a guide. Referring back, Fig. 5.1 shows qualitatively the relationship between entrance currents, I_E, and collector currents, I_C. The flatter the entrance currents are, the more stable the collector current peaks. If an increase in entrance currents is measured, a corresponding increase in collector peaks is also observed. Since the entrance grids are biased at -200V, they should be measuring the ion saturation cur-

rent, $I_{is} = 0.25 e n_e A c_s$. A change in local plasma density, n_e, would be observed through the ion saturation current. Therefore, time windows for each shot were chosen according to where I_{is} was flattest.

In this shot, the entrance currents are relatively flat over 2 time ranges. The range with the lower magnitude is deemed a better choice, however, because not only has the collector current peaks increased over the second range, but the zero point is lower and much less stable. This is graphically similar to the "abnormal mode" observed on many RFAs characterized by the generation of large negative collector currents [18, 20, 13]. While the reasons behind this behaviour are not known, it is observed on JET with a higher plasma density. As just discussed, a higher entrance current could be indicative of higher local plasma density, so it is possible that the second stable range for this shot would provide less meaningful data. To avoid that possibility, the first flat range is chosen for shot 15433, indicated in Fig. 5.1 by vertical dashed lines.

The averaging process itself is one that amalgamates all the current and voltage values for the given time window. For each shot, the voltages are put in 1V "bins". The voltage scan was typically from $V_{scan} \approx$ 7V to 200V. For each temperature measurement, each of the nearly 200 bins was averaged. Each bin, which corresponds to a single data point on the IV curved, had potentially hundreds or thousands of current/voltage data points. Error bars are calculated simply as the standard deviation of all currents in a respective voltage bin. Section 5.2.3 discusses the results of this averaging process.

5.2 Data Analysis

5.2.1 Analysis Methods

Part of the analysis of the data requires curve fitting. In determining ion temperature, the exponential function $I = A + B\exp\left(-(V - V_s)/C\right)$ can be fit to the data, where I is collector current, V is the scanning voltage, and V_s, A, B, and C are free parameters. The ion temperature, in energy units, is represented by C. Alternatively, a linear fit can be made to $\ln(I)$ vs V. The negative reciprocal of the slope provides the ion temperature, again in energy units.

Both methods have different advantages and disadvantages. The primary drawback to fitting a line to the log plot is that the slope is highly affected by the determination of the zero current. In this experiment, the collector currents generally had a DC offset so the method used to define the zero current affected temperature values. The fitting of the exponential function, I, eliminates this issue because the DC offset, A, is determined from the fit. However, a plot of $\log(I)$ vs V shows that above a certain voltage, the data becomes highly chaotic (due to error being higher than ion current). This is less clear from a plot of I vs V.

The choice was made to use the exponential method since, in linear-fitting, the zero-definition of current highly influenced the interpreted temperature. To determine error values for ion temperature, 100 artificial data sets were created with each current value randomly chosen within its respective error bars. The fit was performed each time. From the resulting 100 temperature points, the maximum and minimum values gave us the temperature with its error. This was assumed to mitigate the uncertainty arising from the higher voltage data tail. Figure 5.4 can be referenced as an example. It shows the IV data for shot 15433 including the error bars and was made simply as an example of the exponential fit, and to demonstrate that the data, with relatively small current error, does closely follow an exponential function. The temperature resulting from this fit is noted in the graph. It differs from the above description in that it was created simply using the center current at each voltage point. As just described, each point for an artificial data set should be randomly distributed within the error for that point. The final temperatures for this particular shot are 26.3 ± 1.0 eV and 27.1 ± 1.5 eV for probes A and B, respectively, which include the stated temperatures in Fig. 5.4.

Instrument or other systematic errors were not taken into account. It is expected that these are much less significant than the range created due to the averaging process, especially since, as shown in eq. 2.3, T_i depends on the exponential term rather than the current magnitude itself. Any systematic offset due to measurement error will not influence temperature interpretation.

5.2.2 Flow Measurements

It was mentioned in section 2.2.3 that the actual ion temperature is simply the average of the upstream and downstream measurements. Before temperature can be interpreted from upstream and downstream measurements, it must be shown that this method is accurate for the current

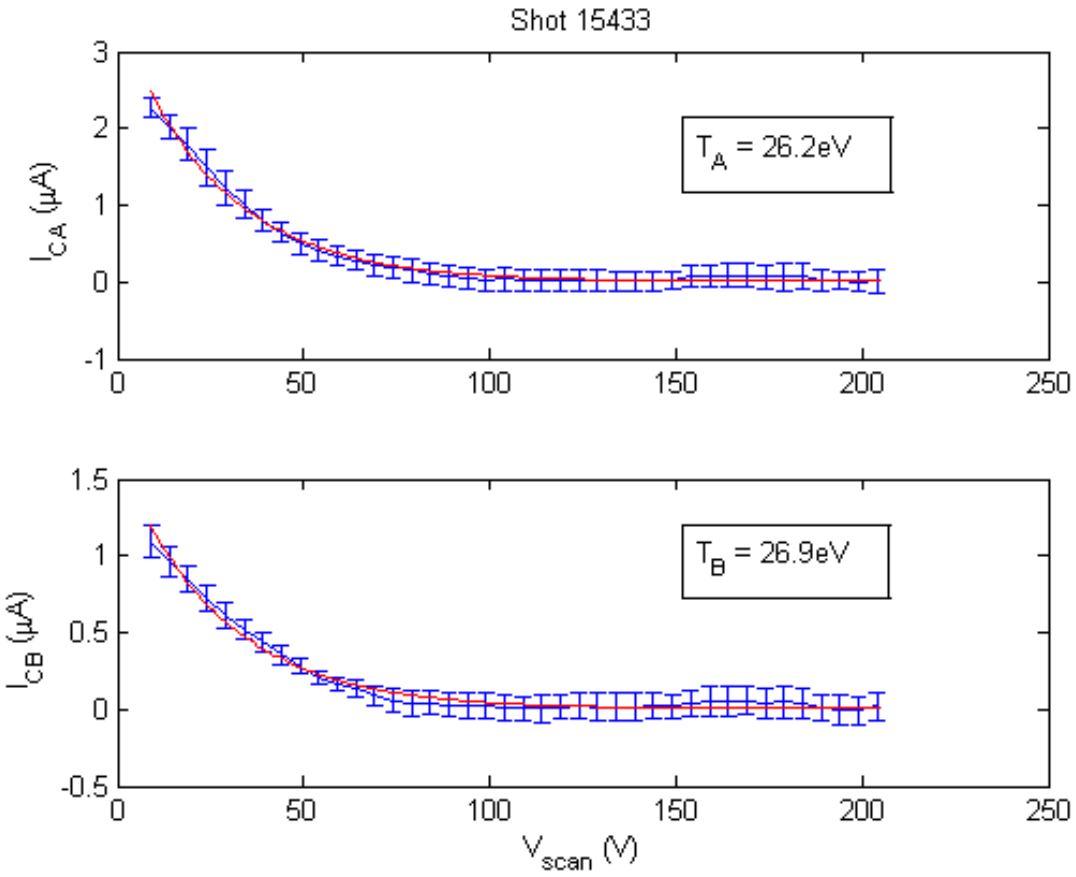

Figure 5.4: Sample of an IV curve from shot 15433. Current error bars are included. Upper plot is probe A, lower plot is probe B. Only every 5th data point is shown in order to make the fitted line more visible.

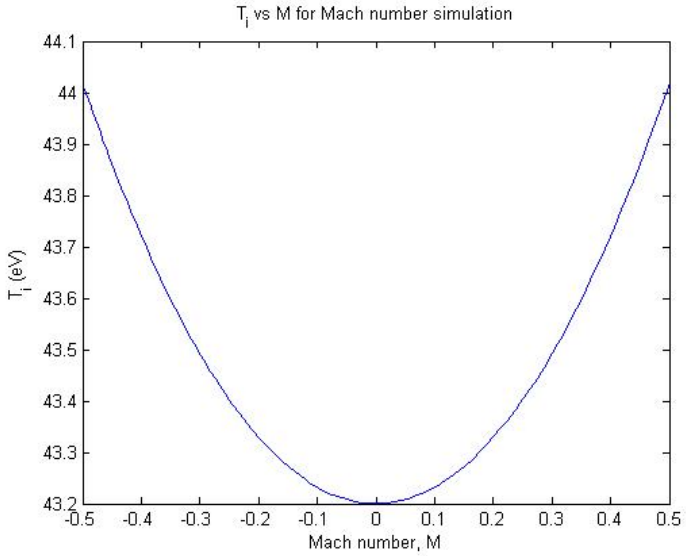

Figure 5.5: T_i vs M where $T_i = (T_+ + T_-)/2$. T_i is plotted in non-normalized units of eV. This shows that for $M < 0.5$, the averaging of T_+ and T_- still provides better than 1eV accuracy and better than 0.1eV accuracy for $M =$ 0.13 to 0.12eV.

situation.

An analytical relationship describing how the upstream and downstream measurements are influenced by plasma flow is used.[9]

$$T_\pm(\phi_s) = \tau \pm U_0\sqrt{\frac{\pi\tau}{2}}\left(\mathrm{erf}\left(\frac{\pm U_0}{\sqrt{2\tau}} - \sqrt{\frac{\phi_s}{\tau}}\right) + 1\right)\exp\left(\frac{\left(\sqrt{2\phi_s} \mp U_0\right)^2}{2\tau}\right) \tag{5.1}$$

where upstream and downstream temperatures are T_+ and T_-, respectively, τ is the real ion temperature, and ϕ_s is the energy difference between the maximum scan (≈225V here) and the entrance biasing (≈-200V). These are all normalized to the electron temperature. Finally, $U_0 = M\sqrt{1+\tau}$, where M is the Mach number. It can be seen that if $M = 0$ then $T_+ = T_- = \tau$. Clearly, both upstream and downstream temperatures are measuring the actual ion temperature, and an average would be exact. However, as M increases, the second term becomes non-zero. Using this relationship, a plot of $T_i = (T_+ + T_-)/2$ vs M is made in Fig. 5.5. For this plot, data from shot 15544 is used because this shot has the highest T_+/T_- ratio. In this shot $T_e = 29.2$eV and $T_i = 43.2 \pm 1.9$eV. The error in T_i is not taken into account for this figure because the shape of the graph is only very weakly affected by it.

To determine M, the entrance grid currents were measured. They were biased at ≈-200V

to ensure that the ion saturation currents were measured. The Mach number can be determined from these measurements using a relationship provided by Chung and Hutchinson[21]. Rearranging it to solve for the Mach number:

$$M = \frac{\ln R}{K}\sqrt{\frac{T_e}{T_e + \gamma_i T_i}} \tag{5.2}$$

where R is the current ratio between upstream and downstream entrance grids (in this case, side B is upstream of side A), T_i is the actual ion temperature, K is a constant defined by Chung and Hutchinson (in this case, $K \approx 1.5$), and γ_i is the specific heat of the ion gas. As discussed by Chung and Hutchinson, it is not obvious what this value should be. They assumed it to be 1, but it could be closer to 2.5. Here, it was taken as 1 to find the maximum Mach number. The current ratio for the time window of shot 15544 is 1.34. From this equation, $M = 0.12$ to 0.13 if δT_i is considered. Referring back to Fig. 5.5, a Mach number of this value affects the results by less than 0.1eV, therefore, averaging upstream and downstream temperatures is considered valid for this experiment.

5.2.3 Multi-shot profile

As mentioned earlier, ion temperature in this section is averaged for the whole time window of a single shot when the RFA is placed at the deepest position for an extended period of time. Depending on the time window chosen for a particular shot, as described above, data from as few as 4 voltage measurements up to about 20 was averaged. Given that each voltage scan period produces 2 measurements (one scanning up and one scanning down), and with a 100Hz source (fully rectified from 50Hz), this corresponds to a time averaging of 20 to 100 ms.

Figure 5.6 shows a plot of the ion temperatures from probes A and B separately. There are a couple interesting characteristics to notice about this plot. The first is that probe B reports a temperature gradient. The temperatures from probe A are pretty consistent. And, at decreasing radial positions, probe B reports a significantly higher temperature than probe A. As previously mentioned, the presence of a plasma flow can be seen by a difference between upstream and downstream temperatures. In the region outside about 41cm, there is no significant difference between either measurement indicating a low Mach number. Closer to the scrape off layer,

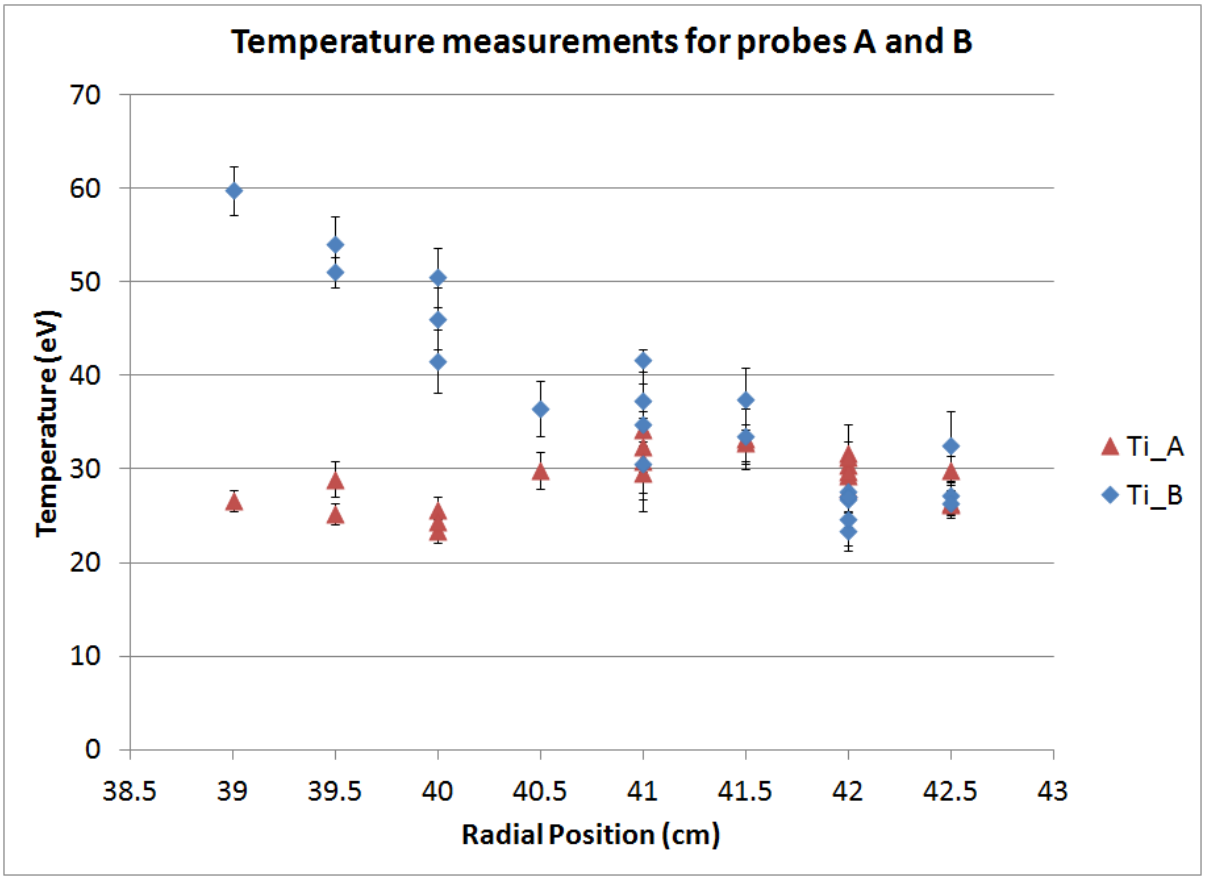

Figure 5.6: T_i profile for 22 different shots for each probe A and probe B. Each data point corresponds to the data for a single shot.

however, an increase in T_i from probe B was noticed, indicating the presence of a noticeable flow in the plasma.

Figure 5.7 shows the ratio of T_{iA} to T_{iB}. Again, at $r = 41$cm and beyond, T_{iA}/T_{iB} can be 1, indicating only a small plasma flow, except perhaps at 42cm for a few of the 6 sample shots at that radial position. Since, however, this profile was assembled from many different shots, there could be turbulent flows present in some shots that are not present at others. In spite of this, there is still a consistent pattern that with lower r comes a greater difference between upstream and downstream temperatures, indicating a greater flow.

It has also been noticed that the ion temperature is consistently higher than electron temperature as shown in Fig. 5.8. The electron temperature profile was measured using an electrical probe mounted on another reciprocating drive at the same radial position as the RFA. It provided electron temperatures in real time, so to be able to compare with RFA data, the electron

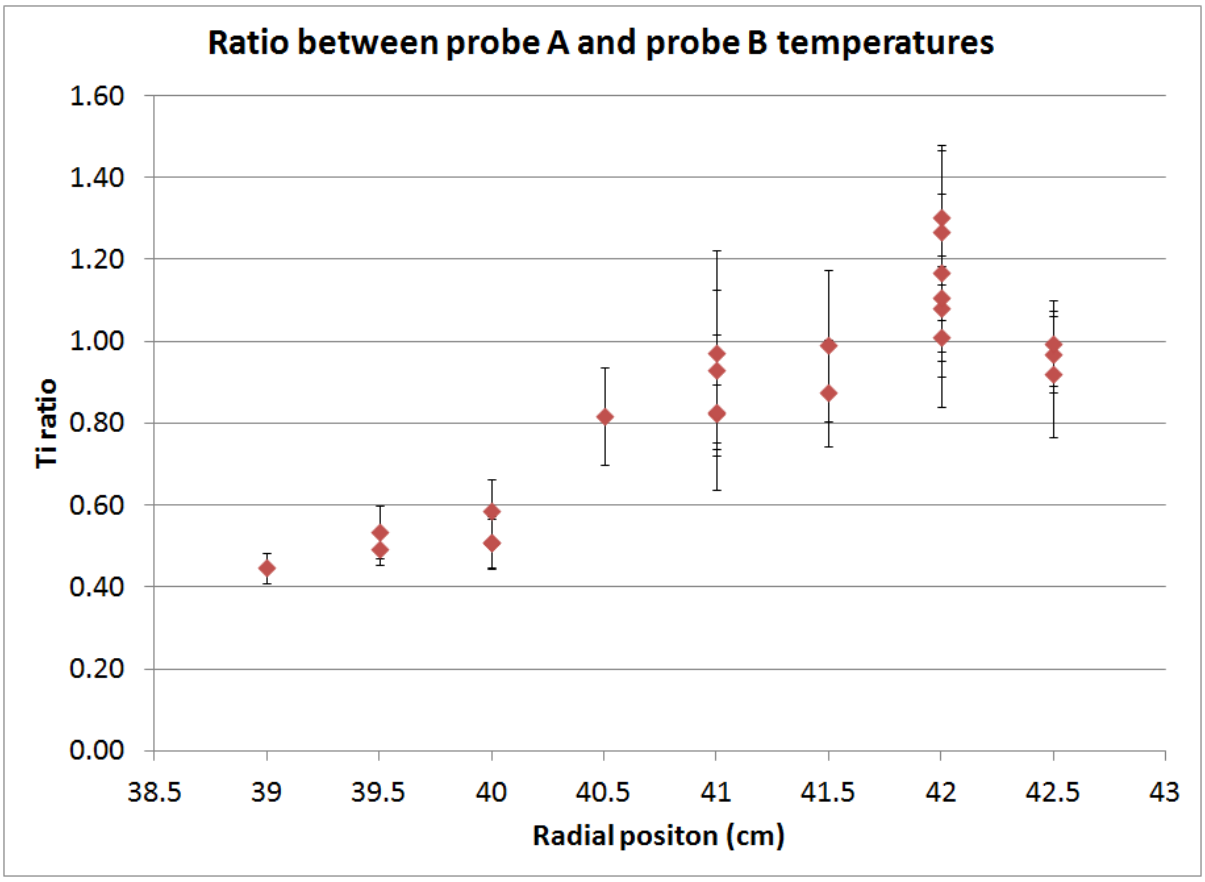

Figure 5.7: Plot of the ratio between probe A and probe B T_i measurements

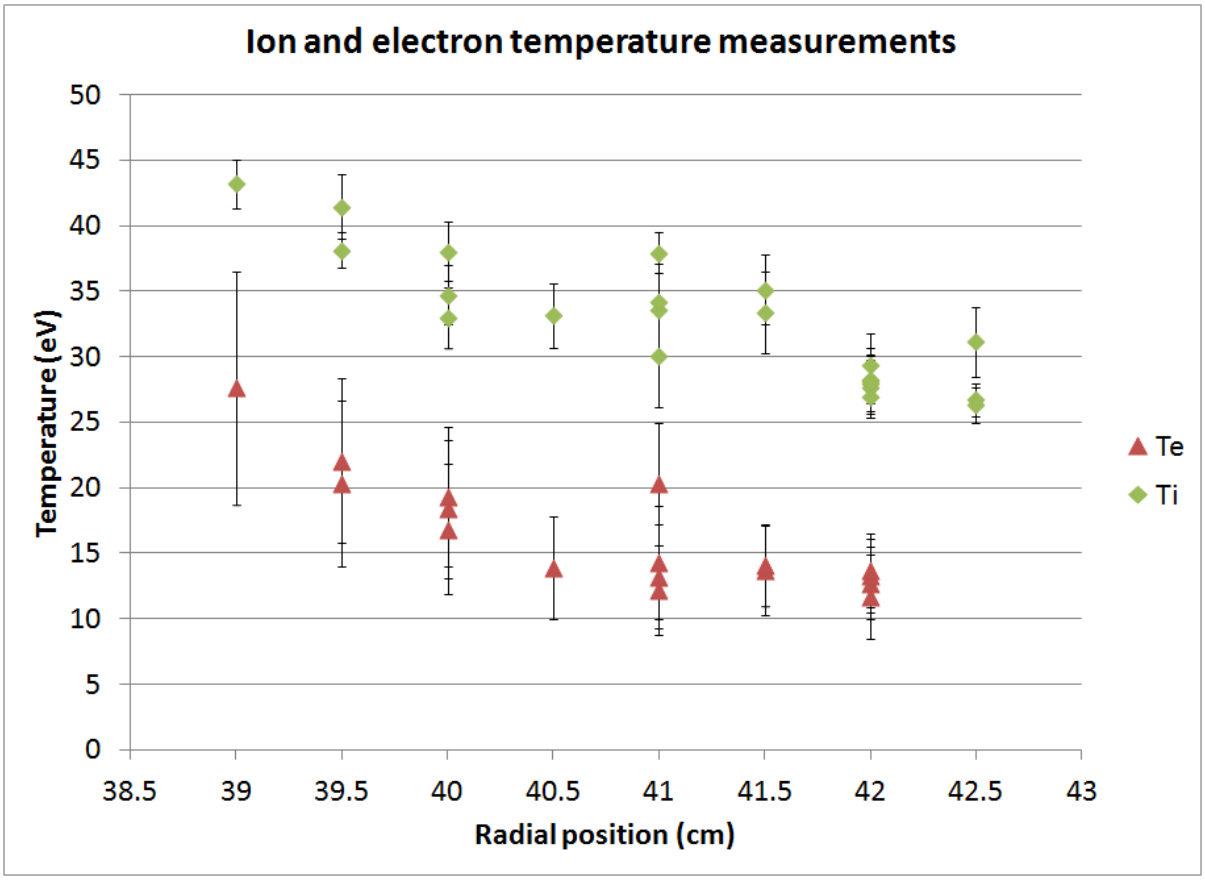

Figure 5.8: T_i and T_e profiles for 21 different shots.

temperature was averaged over the same time period. The error bars for T_e in Fig. 5.8 are calculated using the standard deviation of the T_e measurement.

In the multi-shot ion profile of Fig. 5.9, ion temperature is anywhere from about 1.0 to 3.5 times higher than electron temperature. Given that the plasma edge was at about 37.5cm for each of the 22 shots included in Fig. 5.9, the ratio r/a is within the range of 1.04 to 1.12. In a presentation made at the 19th PSI conference [22], Fig. 5.10 shows the range of T_i/T_e that many other RFA instruments have reported. The highlighted area in green has been added here to show where approximately the results from this experiment would be. It is clear that they fall within the range of other experiments.

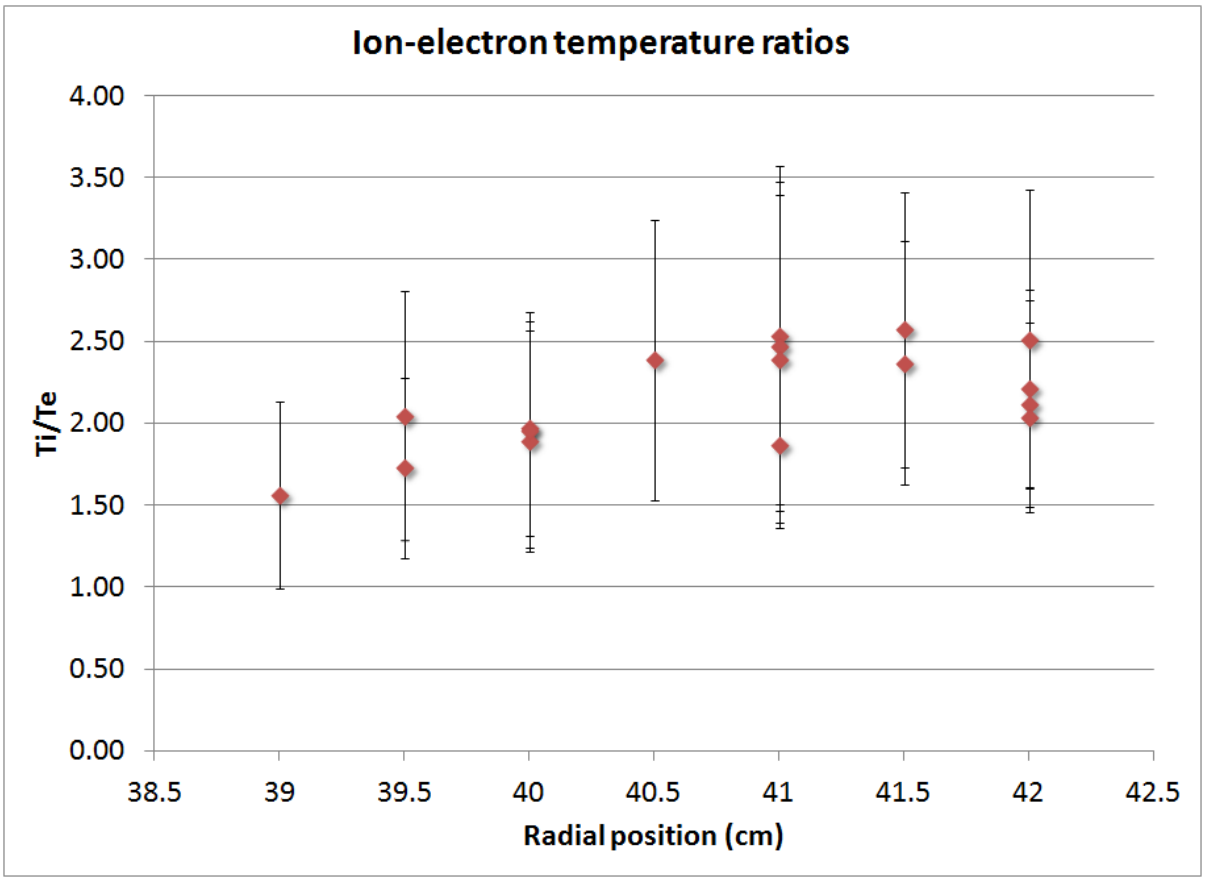

Figure 5.9: Profile with T_i normalized to T_e

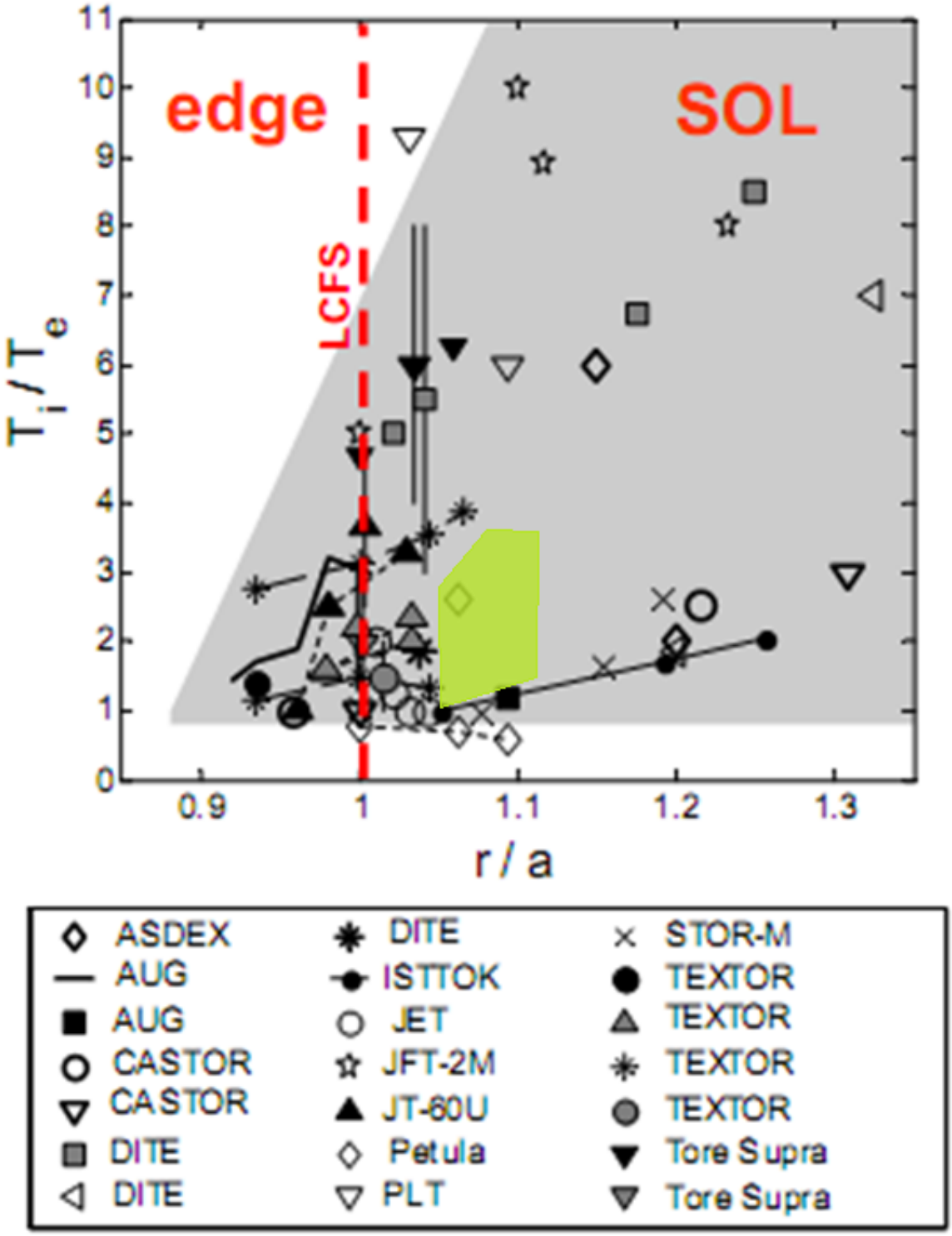

Figure 5.10: Collected RFA temperature ratios for many tokamaks. The approximate range of data from this experiment is highlighted in green.

5.2.4 Single-shot profile

Using shot 15558, a profile across about 2 cm was assembled. Figure 5.11 presents the measurements of position and collector current for this shot with the vertical dotted lines showing the time range over which the ion temperature profile was calculated. The shot characteristics over the time range are quite similar to Fig. 5.1, with the exception that as the probe withdraws from the plasma, one can see all current measurements drop. As the probe moves out of the plasma, all current signals decrease. In the ≈90ms of the scan, 19 measurements were taken.

The assembled profile is plotted in Fig. 5.12. There are no error bars because no scan-averaging was done so no voltage binning was needed. The exponential function was simply fitted to a smoothed, noise-reduced IV plot for a single scan. The ascending scans have been distinguished from the descending ones to highlight the fact that, for nearly all the points, the ascending scans report significantly lower temperature measurements. Unless there is some unknown plasma process that is occurring at the same frequency and phase as the voltage scan, which is highly unlikely, this can only arise from the affect of the probe. The reason for this phenomenon is unknown.

While the quality of the single-shot profile is significantly reduced compared to the multi-shot profile, it still shows some valuable features. If the measurements from both probes for the ascending and descending scans are compared separately, it is seen that for $r < 41.8$cm, probe B reports higher values. The multi-shot profile of Fig. 5.6 also shows that probe B generally reports higher temperatures below 42cm. Also, 3 of the 4 traces from Fig. 5.12 indicate a decreasing temperature with increasing radial distance. Unfortunately, the electron temperature profile was not measured for the current shot.

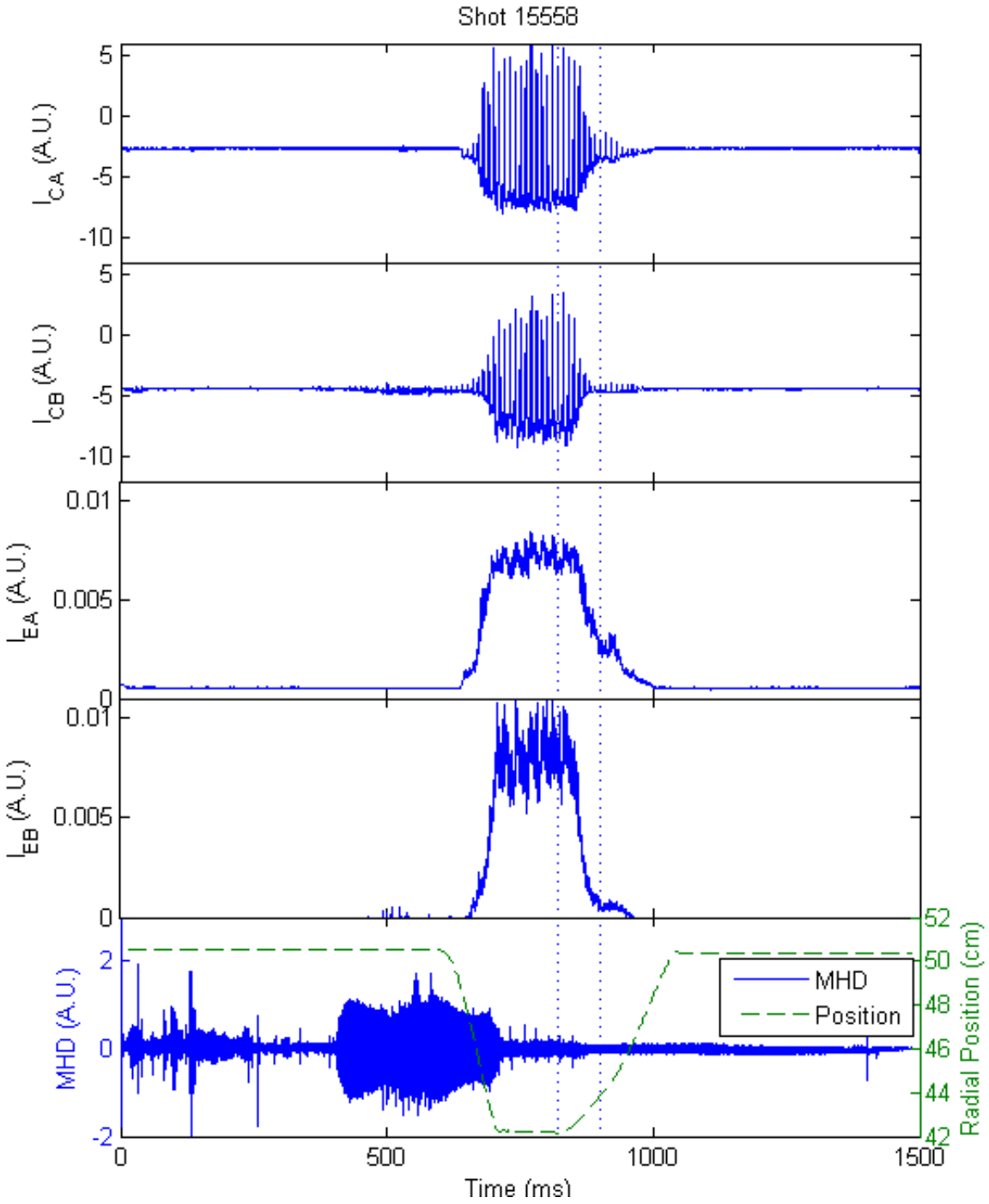

Figure 5.11: Shot conditions for shot 15558. Collector current A and B are shown in the first 2 plots, respectively. Plots 3 and 4 show entrance currents for both probes. The last plot is the position and the MHD signal. The time range for this shot, indicated again in blue dotted lines, show that the profile is made during the probe retraction.

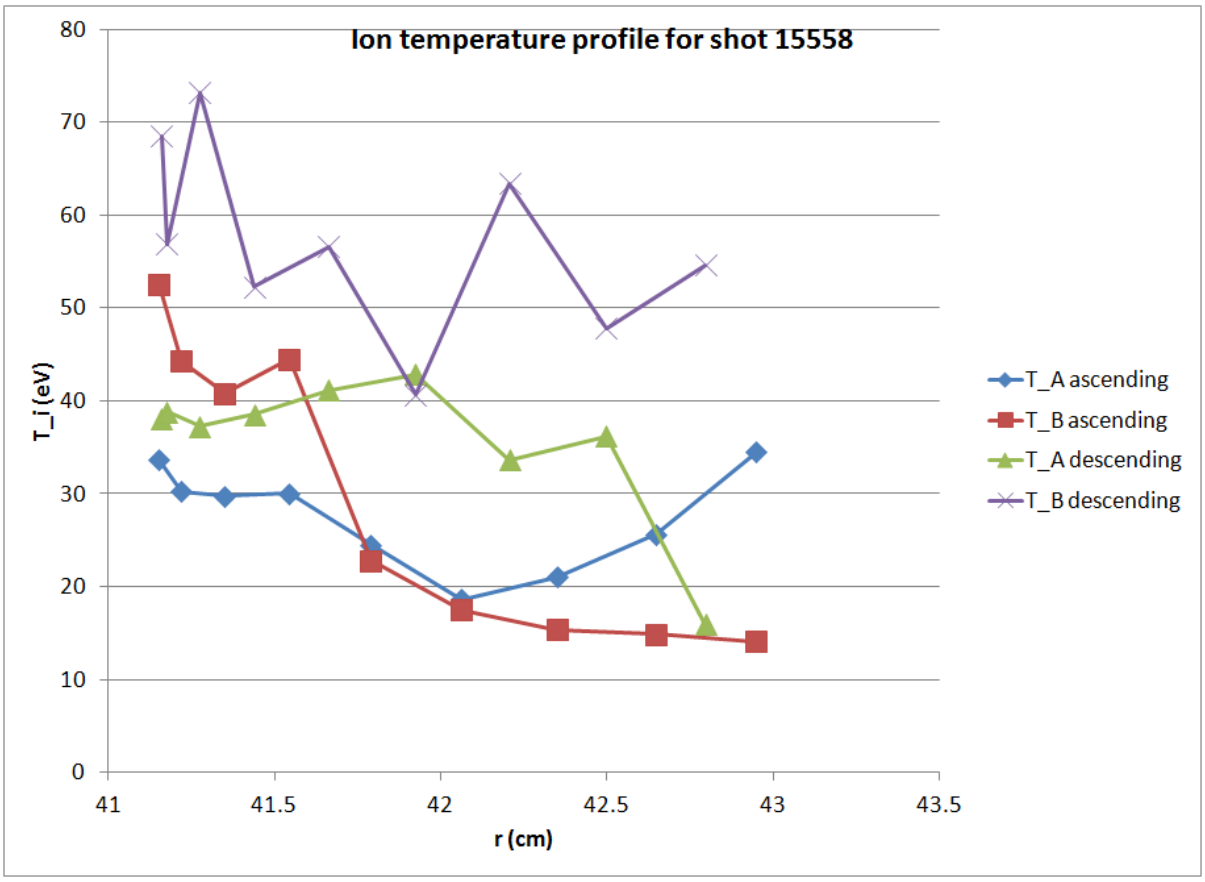

Figure 5.12: Profile from shot 15558. Measurements from the ascending voltage scans are distinguished from the descending measurements to highlight the consistent difference.

CHAPTER 6

CONCLUSION AND FUTURE WORK

Ion temperature in the edge region of the tokamak plasma is a key value potentially providing insight into edge plasma features that are responsible for the H-mode discovered in tokamaks. This H-mode is characterized by a dramatic increase in plasma stability and confinement times when compared with L-mode. More knowledge of this phenomenon could enable the construction of a tokamak capable of a self-sustain fusion reaction.

An RFA was designed and implemented on the HL-2A tokamak in Chengdu, China. Measuring ion temperature, it provided qualitative and quantitative agreement with RFA theory and past RFA experiments. A collection of 22 shots was used to assemble an ion temperature profile from $r = 38.5$ to 42.5cm where the plasma edge is $a \approx 37.5$cm. Combined with electron temperature data taken at the same location for most of the same shots, it was possible to investigate the relationship between the two. As measured on many RFAs in the past on differing machines, ion temperature is consistently measured higher than electron temperature. While the reason for this is not completely explained, because that phenomenon was seen here demonstrates that this RFA worked sufficiently well within typical RFA expectations to provide meaningful results.

The primary benefit of an oscillating probe drive is the potential of achieving an ion temperature profile from a single shot. This, too, was achieved in this experiment, further verifying the RFA's ability for shot-dependent ion profiles. However, the single-shot profile has some weaknesses compared with the multi-shot profile. It is both narrower and farther in the scrape-off layer. Also, over the several hundred shots examined, no ion temperature measurements were taken within the separatrix. Some reasons identified for these limitations are due to the mechanical design of the probe. It was possible to reduce the plasma-facing profile of the probe, as well as to reduce the distance from the top of the probe body to the probe entrance.

Both of these were drastically improved in a second design. The second version of the RFA is expected to provide better single shot performance, probing deeper into the plasma while destabilizing it less. With these successes, and the potential for a much improved experiment on the next probe, it is hoped that specific machine time could be devoted to the RFA probe on a future experiment at EAST.

A few examples of unexplained behaviour were noted. One of them pertains to the single shot profile. For an unknown reason, when the voltage scan went from minimum to maximum, the reported temperature was consistently lower than when the voltage scan returned from maximum to minimum. Also, all the currents measured and examined - the 2 entrance currents and the 2 collector currents - had a shot-dependent DC drift associated with it. For the purposes of examining the data, it was numerically removed. However, it might be caused by something affecting the temperature measurement itself. No anomalies were noted in the temperature data, but given that the RFA is still not very well verified externally, this should be investigated.

Additionally, current traces from probe B reported stronger signals than those from probe A. In other probes, such as the JET experiment, this was noticed in the upstream probe. However, in this experiment, it was always noticed in the same probe, regardless of the direction of the plasma flow for that shot. Again, the causes for this are not known.

Finally, noise was an ever-present concern. Many of the individual scans were unable to provide reliable temperature values. Part of this is due to the inconsistent plasma conditions afforded during experiment time. The addition of a dummy wire allowed interference to be considerably reduced, but it is expected that further reduction can be achieved with more attention paid to isolation in the wires. The JET experiment used triaxial cables rather than the coaxial cables used in this experiment.

A theoretical model was developed to investigate the affect of probe geometry on temperature measurements. Inputting the geometry for the current probe with $M \leq 0.13$, measured values are accurate within 5%. While the model does make some simplifying assumptions, they are expected to represent an upper bound on the temperature over-estimation. As far as the author knows, there are no published accounts of attempts to model the affect of probe geometry in this way. The results here are interesting enough to warrant further investigation.

Overall, while some obvious areas were identified that need to be addressed in order to

improve the quality of the RFA data, the data provided by this experiment is in agreement with previous RFA measurements on different tokamak machines. A second RFA has been made whose design improves on some of the identified weaknesses of the current experiment. It is hoped that this updated probe can be implemented on the superconducting EAST tokamak in Hefei in the near future.

BIBLIOGRAPHY

[1] U. E. I. Administration, "International Energy Annual 2006," http://www.eia.gov/countries/data.cfm. date accessed: June 10, 2012.

[2] U. E. I. Administration, http://www.eia.gov/oiaf/1605/ggccebro/chapter1.html. date accessed: June 10, 2012.

[3] M. S. Prasad and K. Kumari, "Toxicity of crude oil to the survival of fresh water fish *Puntius sophore* (ham.)," *Acta hydrochimica et hydrobiologica*, vol. 15, 1987.

[4] C. Baker, "Tokamak Reactor Studies," *Proceedings of the IEEE*, vol. 69, 1981.

[5] R. J. Bickerton, "History of the approach to ignition," *Philosophical Transactions of the Royal Society A*, vol. 357, pp. 397–413, 1999.

[6] F. F. Chen, *Plasma Physics and Controlled Fusion*. Springer, 2006.

[7] K. Miyamoto, *Plasma Physics and Controlled Nuclear Fusion*. Springer, 2005.

[8] M. Kocan, J. P. Gunn, J.-Y. Pascal, and E. Gauthier, "Ion temperature measurements in the tore supra scrape-off layer using a retarding field analyzer," *Contributions to Plasma Physics*, vol. 50, 2010.

[9] F. Valsaque, G. Manfredi, J. P. Gunn, and E. Gauthier, "Kinetic simulations of ion temperature measurements from retarding field analyzers," *Physics of Plasmas*, vol. 9, no. 5, 2002.

[10] G. McKee, P. Gohil, D. Schlossberg, J. Boedo, K. Burrell, J. deGrassie, R. Groebner, R. Moyer, C. Petty, T. Rhodes, L. Schmitz, M. Shafer, W. Solomon, M. Umansky, G. Wang, A. White, and X. Xu, "Dependence of the L- to H-mode power threshold on toroidal rotation and the link to edge turbulence dynamics," *Nuclear Fusion*, vol. 49, 2009.

[11] T. Ido, Y. Miura, K. Kamiya, Y. Hamada, K. Koshino, A. Fujisawa, K. Itoh, S.-I. Itoh, A. Nishizawa, H. Ogawa, and Y. Kusama, "Geodesic-acoustic-mode in jft-2m tokamak plasmas," *Plasma Physics and Controlled Fusion*, vol. 48, no. 4, 2006.

[12] K. H. Burrell, E. J. Doyle, P. Gohil, R. J. Groebner, J. Kim, R. J. L. Haye, L. L. Lao, R. A. Moyer, T. H. Osborne, W. A. Peebles, C. L. Rettig, T. H. Rhodes, and D. M. Thomas, "Role of the radial electric field in the transition from L(low) mode to H(high) mode to VH(very high) mode in the DIII-D tokamak," *Physics of Plasmas*, vol. 1, 1994.

[13] R. A. Pitts, R. Chavan, S. J. Davies, S. K. Erents, G. Kaveney, G. F. Matthews, G. Neill, J. E. Vince, and I. Duran., "Retarding field energy analyzer for the JET plasma boundary," *Review of Scientific Instruments*, vol. 74, no. 11, pp. 4644–4657, 2003.

[14] I. Katsumata and M. Okazaki, "Ion Sensitive Probe - A New Diagnostic Method for Plasma in Magnetic Fields," *Japan Journal of Applied Physics*, vol. 6, 1967.

[15] N. Ezumi, "PIC Simulations of the Motion of Plasma around Ion sensitive Probes," *Contributions to Plasma Physics*, vol. 41, 2001.

[16] G. Matthews, "Tokamak plasma diagnosis by electrical probes," *Plasma Physics and Controlled Fusion*, vol. 36, 1994.

[17] K. Uehara, T. Kawakami, H. Amemia, K. Hoethker, A. Cosler, and W. Bieger, "Measurements of ion temperature and flow felocity using symmetric and asymmetric double probes in the boundary plasma of the JFT-2M tokamak," *Nuclear Fusion*, vol. 38, 1998.

[18] M. Dreval, D. Rohraff, C. Xiao, and A. Hirose, "Retarding field energy analyzer for the Saskatchewan Torus-Modified plasma boundary," *Review of Scientific Instruments*, vol. 80, 2009.

[19] M. Kocan, J. P. Gunn, M. Komm, J.-Y. Pascal, E. Gauthier, and G. Bonhomme, "On the reliability of scrape-off layer ion temperature measurements by retarding field analyzers," *Review of Scientific Instruments*, vol. 79, 2008.

[20] I. S. Nedzelskiy, C. Silva, H. Fernandes, and C. A. F. Varandas, "Compact retarding field energy analyzer for the tokamak ISTTOK boundary plasma," *Review of Scientific Instruments*, vol. 77, 2006.

[21] K.-S. Chung and I. H. Hutchinson, "Kinetic theory of ion collection by probing objects in flowing strongly magnetized plasmas," *Physical Review A*, vol. 38, 1988.

[22] M. Kocan, J. Gunn, S. Carpentier-Chouchana, A. Herrmann, A. Kirk, M. Komm, H. Müller, J.-Y. Pascal, R. Pitts, V. Rohde, and P. Tamain, "Measurements of ion energies in the tokamak plasma boundary," in *Proceedings of the 19th International Conference on Plasma-Surface Interactions in Controlled Fusion*, vol. 415, 2011.